

REPORT DOCUMENTATION PAGEForm Approved
OMB NO. 0704-0188

Public Reporting burden for this collection of information is estimated to average 1 hour per response, including the time for reviewing instructions, searching existing data sources, gathering and maintaining the data needed, and completing and reviewing the collection of information. Send comment regarding this burden estimate or any other aspect of this collection of information, including suggestions for reducing this burden, to Washington Headquarters Services, Directorate for Information Operations and Reports, 1215 Jefferson Davis Highway, Suite 1204, Arlington, VA 22202-4302, and to the Office of Management and Budget, Paperwork Reduction Project (0704-0188), Washington, DC 20503.

1. AGENCY USE ONLY (Leave Blank)		2. REPORT DATE 05/23/2008		3. REPORT TYPE AND DATES COVERED Final Report	
4. TITLE AND SUBTITLE Understanding Energy Absorption Behaviors of Nanoporous Materials				5. FUNDING NUMBERS W911NF-07-1-0070 (ORSSP Proposal #: R6868)	
6. AUTHOR(S) Yu Qiao					
7. PERFORMING ORGANIZATION NAME(S) AND ADDRESS(ES) The University of California, San Diego 9500 Gilman Dr., MC 0085, La Jolla, CA 92093-0085				8. PERFORMING ORGANIZATION REPORT NUMBER The University of California, San Diego	
9. SPONSORING / MONITORING AGENCY NAME(S) AND ADDRESS(ES) U. S. Army Research Office P.O. Box 12211 Research Triangle Park, NC 27709-2211				10. SPONSORING / MONITORING AGENCY REPORT NUMBER	
11. SUPPLEMENTARY NOTES The views, opinions and/or findings contained in this report are those of the author(s) and should not be construed as an official Department of the Army position, policy or decision, unless so designated by other documentation.					
12 a. DISTRIBUTION / AVAILABILITY STATEMENT Approved for public release; distribution unlimited.				12 b. DISTRIBUTION CODE	
13. ABSTRACT (Maximum 200 words) With the support of ARO through Grant No. W911NF-04-1-0244, the energy absorption behaviors of nanoporous materials are being investigated systematically. The significant achievements include: (1) validating the concept of the use of nanoporous materials in energy absorption systems; (2) identifying the optimum surface species; (3) performed preliminary high-strain-rate experiment; (4) developed systems based on viscous liquids such as glycerin, so that the beneficial internal friction effect and shear thickening effect can be maximized; (5) identified suitable nanoporous materials; (6) analyzed energy generation associated with infiltration of ionic liquids; (7) applied the NMF liquids in honeycomb structures; (8) analyzed the direct compression of nanoporous frameworks; and (9) developed models to better understand the behaviors of pressurized nanofluids.					
14. SUBJECT TERMS				15. NUMBER OF PAGES	
				16. PRICE CODE	
17. SECURITY CLASSIFICATION OR REPORT UNCLASSIFIED	18. SECURITY CLASSIFICATION ON THIS PAGE UNCLASSIFIED	19. SECURITY CLASSIFICATION OF ABSTRACT UNCLASSIFIED	20. LIMITATION OF ABSTRACT UU		

REPORT DOCUMENTATION PAGE (SF298)
(Continuation Sheet)

I. Publications Supported by The Army Research Office

(a) Publications in Peer Reviewed Journals:

1. Han, A.; Punyamurtula, V. K.; Qiao, Y. Heat generation associated with pressure induced infiltration in a nanoporous silica gel. *J. Mater. Res.*, in the press.
2. Han, A.; Qiao, Y. Influence of surface treatment on defiltration of confined liquid in MCM-41. *Chem. Phys. Lett.*, in the press.
3. Han, A.; Punyamurtula, V. K.; Kim, T.; Qiao, Y. The upper limit of energy density of nanoporous materials functionalized liquids. *J. Mater. Eng. Perform.*, in the press.
4. Punyamurtula, V. K.; Han, A.; Qiao, Y. Pressurized flow in a mesostructured silica modified by silane groups. *J. Fluids Eng. – Trans. ASME*, in the press.
5. Han, A.; Punyamurtula, V. K.; Qiao, Y. Effects of cation size on infiltration and defiltration pressure of a MCM-41. *Appl. Phys. Lett.* **92**, 153117.1-3 (2008).
6. Han, A.; Punyamurtula, V. K.; Lu, W.; Qiao, Y. Deformation of a nanoporous silica under compressive loading. *J. Appl. Phys.* **103**, 084318.1-5.
7. Han, A.; Punyamurtula, V. K.; Qiao, Y. Effects of decomposition-treatment temperature on infiltration pressure of a surface-modified nanoporous silica gel. *Chem. Eng. J.* **139**, 426-429 (2008).
8. Han, A.; Punyamurtula, V. K.; Qiao, Y. Infiltration of liquid metals in a nanoporous carbon. *Phil. Mag. Lett.* **88**, 67-73 (2008).
9. Punyamurtula, V. K.; Qiao, Y. A selectively-energy-absorbing nanoporous system. *Mater. Lett.* **62**, 2928-2930 (2008).
10. Qiao, Y.; Cao, G.; Chen, X. Effects of gas molecules on nanofluidic behaviors. *J. Am. Chem. Soc.* **129**, 2355-2359 (2007).
11. Han, A.; Qiao, Y. Effects of surface treatment of a MCM-41 on motions of confined liquids. *J. Phys. D – Appl. Phys.* **40**, 5743-5746 (2007).
12. Punyamurtula, V. K.; Han, A.; Qiao, Y. Damping properties of nanoporous carbon – cyclohexane mixtures. *Adv. Eng. Mater.* **9**, 209-211 (2007).
13. Han, A.; Qiao, Y. Controlling infiltration pressure of a nanoporous silica gel via surface treatment. *Chem. Lett.* **36**, 882-883 (2007).
14. Punyamurtula, V. K.; Qiao, Y. Infiltration of pressurized promoter solutions in a mesoporous silica. *Microporous Mesoporous Mater.* **103**, 35-39 (2007).
15. Han, A.; Qiao, Y. Suppression effect of liquid composition on defiltration of nanofluids in lyophobic environment. *J. Phys. D – Appl. Phys.* **40**, 3436-3439.
16. Punyamurtula, V. K.; Qiao, Y. Hysteresis of sorption isotherm of a multiwall carbon nanotube in paraxylene. *Mater. Res. Innov.* **11**, 37-39 (2007).
17. Chen, X., Surani, F. B., Kong, X., Punyamurtula, V. K., and Qiao, Y. Energy absorption performance of steel tubes enhanced by nanoporous material functionalized liquid. *Appl. Phys. Lett.* **89**, 241918.1-3 (2006).

18. Surani, F. B., Han, A., and Qiao, Y. An experimental investigation on pressurized liquid in confining nanoenvironment. *Appl. Phys. Lett.* **89**, 093108.1-3 (2006).
19. Punyamurtula, V. K., Han, A., and Qiao, Y. An experimental investigation on a nanoporous carbon functionalized liquid damper. *Phil. Mag. Lett.* **86**, 829-835 (2006).
20. Kong, X., Falgun, F. B., and Qiao, Y. Energy Absorption of nanoporous silica particles in aqueous solutions of sodium chloride. *Phys. Scripta* **74**, 531-534 (2006).
21. Han, A. and Qiao, Y. Pressure induced infiltration of aqueous solutions of multiple promoters in a nanoporous silica. *J. Am. Chem. Soc.*, **128**, 10348 (2006).
22. Surani, F. B., Han, A., and Qiao, Y. Thermal recoverability of a polyelectrolyte modified nanoporous silica based system. *J. Mater. Res.* **21**, 2389 (2006).
23. Surani, F. B. and Qiao, Y. Infiltration and defiltration of an electrolyte solution in nanopores. *J. Appl. Phys.* **100**, 034311 (2006).
24. Surani, F. B. and Qiao, Y. An energy absorbing polyelectrolyte gel matrix composite material, *Compos. A* **37**, 1554 (2006).
25. Han, A., Kong, X., and Qiao, Y. Pressure induced liquid infiltration in nanopores. *J. Appl. Phys.* **100**, 014308.1-3 (2006).
26. Surani, F. B. and Qiao, Y. Energy absorption of a polyacrylic acid partial sodium salt modified nanoporous system, *J. Mater. Res.* **21**, 1327-1330 (2006).
27. Surani, F. B. and Qiao, Y. Pressure induced infiltration in an epsomite-silica system. *Phil. Mag. Lett.* **86**, 253-260 (2006).
28. Surani, F. B. and Qiao, Y. Pressure induced infiltration in a functionalized poly(acrylic acid-co-acrylamide) potassium salt gel matrix material, *Mater. Res. Innov.* **10**, 129-137 (2006).
29. Surani, F. B., Kong, X., and Qiao, Y. Two-staged sorption isotherm of a nanoporous energy absorption system, *Appl. Phys. Lett.* **87**, 251906.1-3 (2005).
30. Kong, X. and Qiao, Y. Improvement of recoverability of a nanoporous energy absorption system by using chemical admixture, *Appl. Phys. Lett.* **86**, 151919.1-3 (2005).
31. Surani, F. B., Kong, X., Panchal, D. B., and Qiao, Y. Energy absorption of a nanoporous system subjected to dynamic loadings, *Appl. Phys. Lett.* **87**, 163111.1-3 (2005).
32. Kong, X., Surani, F. B., and Qiao, Y. Effects of addition of chemical admixtures on the infiltration pressure of a mesoporous silica, *J. Mater. Res.* **20**, 1042-1045 (2005).
33. Kong, X. and Qiao, Y., Thermal effect on pressure induced infiltration of a nanoporous system, *Phil. Mag. Lett.* **85**, 331-337 (2005).
34. Qiao, Y. and Kong, X., Effective dewetting in a microporous particle, *J. Fluids Eng. – Trans. ASME*, **127**, 1128-1131 (2005).
35. Qiao, Y., Kong, X., Chakravarthula, S. S. An analysis of aggregate response of confined liquids in nanoenvironments, *J. Math. Chem.*, **37**, 93-99 (2005).
36. Qiao Y, Kong X. Modeling of the kinetics of confined nonwetting flow in a mesoporous particle. *Phys. Scripta*, **71**, 27-30 (2005).

(b) Presentations

1. Qiao, Y., Han, A. Advanced energy conversion techniques using nanoporous materials. *ASCE Earth & Space 2008*, Long Beach, CA (March 02-05, 2008). INVITED
2. Qiao, Y., Han, A. Using nanoporous materials for energy conversion. *ASME International Mechanical Engineering Congress & Exposition*, Seattle, WA (November 12-15, 2007).

3. Qiao, Y. Novel applications of nanoporous materials in mechanical systems. *Institute of Mechanics, Chinese Academy of Sciences*, Beijing, China (June 28, 2007). INVITED
4. Qiao, Y. Developing high-performance infrastructure materials using locally harvestable resources. *Department of Engineering Mechanics, Hohai University*, Nanjing, China (June 15, 2007) INVITED
5. Qiao, Y., Han, A. Liquid motion in nanopores. *NSF/Sandia Workshop 2007*. Albuquerque, New Mexico (October 24-26, 2007).
6. Qiao, Y., Punyamurtula, Han, A. Development of liquid dampers. *Materials Science and Technology*, Detroit, MI (September 16-20, 2007)
7. Qiao, Y., Han, A., Punyamurtula, V. K. An energy absorbing composite material functionalized by nanoporous particles. *The 16th International Conference on Composite Materials*, Kyoto, Japan (July 8-13, 2007)
8. Qiao, Y. and Han, A. Smart liquids. *International Conference on Smart Materials and Nanotechnology*, Harbin, China (July 1-4, 2007).
9. Qiao, Y., Han, A. Honeycomb structures enhanced by nanoporous material functionalized liquids. *The 5th International Conference on Nonlinear Mechanics*, Shanghai, China (June 10-14, 2007).
10. Qiao, Y., Han, A. Developing smart liquids based on nanoporous technologies. *The 14th SPIE International Symposium of Smart Structures and Materials & Nondestructive Evaluation and Health Monitoring*, San Diego, California (March 18-22, 2007)
11. Qiao, Y., Han, A., Surani, F. B. Using nanoporous material functionalized liquid to enhance cellular structures. *The 15th US National Congress of Theoretical and Applied Mechanics*, Boulder, Colorado (June 25-30, 2006)
12. Qiao, Y., Han, A., Kong, X. Developing high-performance energy absorption systems using nanoporous materials. *TMS Annual Meeting*, San Antonio, Texas (March 13-16, 2006).
13. Qiao, Y. and Surani, F. B., A novel application of nanoporous materials in energy absorption systems. *ASME Nano Conference: Integrated Nanosystems*, Berkeley, California (September 14-16, 2005)
14. Qiao, Y., Use of nanoporous materials in mechanical systems – an inside story. *Invited Seminar for The Department of Mechanical Engineering, University of Colorado at Boulder*, Boulder, Colorado (August 25, 2005). INVITED
15. Qiao, Y., Surani, F. B., and Kong, X., Developing high-performance energy absorption systems based on nanotechnologies. *The Joint ASCE/ASME/SES Conference on Mechanics and Materials*, Baton Rouge, Louisiana (June 1-3, 2005).

II. Demographic Data for this Reporting Period:

- (a) Number of Manuscripts submitted: 36
- (b) Number of Peer Reviewed Papers submitted: 36
- (c) Number of Non-Peer Reviewed Papers submitted: 0
- (d) Number of Presented but not Published Papers submitted: 15

III. Personnel Involved in the Project

- Yu Qiao, PI, Associate Professor of Materials Science and Structural Engineering
- A. Alice Han, Postdoctoral Scholar
- Lance A. Operhall, Master Student
- Venkata K. Punyamurtula, Taewan Kim, Ph.D. Students

IV. Scientific Achievements

A. Liquid Enhanced Honeycomb and Blast Simulator Testing

Due to its high energy absorption efficiency, cellular structure is one of the most attractive EAMS. Commonly used cellular structures include space filling foams and their two-dimensional counterparts, honeycombs, which are lightweight and can be made with relative ease by all major material categories. In these materials, performance is optimized by geometric arrangement of the solids in space to form interconnected or isolated cells. When compressive loadings are applied, the cell walls can buckle, which is the primary energy absorption mechanism. They are widely applied for shock mitigation, packaging, as well as damping. Honeycomb is one of the most widely applied cellular structures. When being compressed from the lateral direction, the cell walls can deform quite smoothly. However, if the compressive load is applied along the out-of-plane direction, during the buckling process the working load is highly non-uniform. Under this condition, especially in a thin-walled structure, the wavelengths of wrinkles in cell walls are much smaller than the structural size. Initially, as the cell wall is nearly perfect, buckling initiation demands a large stress. As the cell wall becomes locally sigmoidal, the critical stress for the expansion of wrinkled zone becomes much lower. That is, while the cell-wall buckling is activated at a high stress level, the major portion of the energy absorbing process, which dominates the overall energy absorption efficiency, takes place at a relatively low stress level, significantly lowering the overall protection/damping capacity.

One method to solve this problem is to reinforce the honeycomb by a filler, particularly, a liquid filler. The mechanical property of liquid-containing cellular structures has been an active research area. Usually, compared with the network material, the liquid is of a relatively low weight density, and thus the structure is still lightweight. Moreover, the liquid can spontaneously fit well with the cell wall, avoiding possible problems of filler-network mismatch. The thermal, electrical, and magnetic properties of the structure can also be adjusted in broad ranges. However, since most of liquids are nearly incompressible and therefore cannot accommodate cell-wall buckling, the liquid filled honeycombs are often rigid; that is, the major advantage of being cellular is lost. Using nanoporous materials functionalized (NMF) liquids to enhance the honeycomb performance is a promising way to solve this problem.

A major concern of using NMF liquids to enhance honeycombs is related to the pressure difference across the cell wall. In the interior of a honeycomb panel, since the NMF liquid is compressible and the pressure is balanced by adjacent cells, the buckling behavior should be quite similar with that of empty ones. At the lateral surface of the panel, however, there is a large pressure difference can be high. If these cells buckle and fail easily, the overall energy absorption capacity would be relatively low.

In order to validate this concept, particularly to analyze the behaviors of cells at outer surfaces, the experimental setup depicted in Fig.A-1 was developed. The testing system consisted of a thin-walled stainless steel cylinder and a liquid phase sealed in it. The height, outer diameter, and wall thickness of the cylinder were $h = 25.4$ mm, $2R = 6.86$ mm, and $t = 0.13$ mm, respectively. Both ends of the cell were fixed on stainless steel loading plates using a J-B Weld epoxy glue. The cell was filled by an aqueous suspension of 0.4 g of Fluka 100 C₈ reversed phase nanoporous silica gel. The sample preparation was performed under water so that no air was entrapped. The nanoporous silica gel was hydrophobic. The average nanopore size was 7.8 nm. The specific nanopore volume was 0.55 cm³/g. At the infiltration pressure of about 18 MPa, one gram of the silica gel can dissipate about 14 J of energy. The details of the NMF liquid behavior have been documented

elsewhere. The samples were tested using a type 5569 Instron machine. The crosshead speed was set to 0.5 mm/min. For comparison purpose, empty cells and cells filled by distilled water were also tested. For each type of cell, 3-5 samples were analyzed. Figure A-2 shows typical stress-strain curves, where the nominal stress is defined as $P = F/A_0$, and the nominal strain is defined as $\varepsilon = \delta/h$, with F being the applied load, δ the piston displacement, and $A_0 = 36.9 \text{ mm}^2$ the cross-sectional area of the steel cell.

It can be seen clearly that the deformability of the empty cell is quite high. After the initial linear compression stage, as the buckling initiates and continues, a broad plateau is formed, with the width of more than 70% of the initial cell height. As discussed above, due to the change in cell wall configuration, the buckling initiation stress is much higher than the buckling development stress. The buckling plateau is quite jerky, consisting of a number of “bumps”. Each “bump” reflects the stress accumulation, formation, and folding process of a wrinkle.

As the cell is filled by distilled water, since the compressibility of water is negligible, the cell-wall buckling is suppressed, and initially the energy dissipation is dominated by the extended cell-wall yielding along the radius direction. As a result, the system becomes quite rigid, and shortly after the peak load is reached, the inner pressure becomes sufficiently high such that abrupt cracking takes place along the longitudinal direction. After the liquid leaks, the system behavior resembles that of an empty cell, except that, since the crack weakens the cell wall, the buckling of the fractured cell occurs at a relatively low stress level. Depending on the crack length, the decrease in buckling stress is in the range of 5-25%. Therefore, the energy absorption capacity is reduced, as shown in Table A-1, where the absorbed energy, U , is calculated as the average area under the load-displacement curves in the nominal strain range of 0 to 0.75, and m and V are the system mass and the system volume, respectively.

The solid curve in Fig.A-2 indicates the behavior of a cell filled by the NMF liquid. After the initial linear compression section (“OA”), as the critical nominal stress of about 35 MPa is reached the cell wall deforms plastically along the radius direction, since the buckling is suppressed by the liquid phase. As the cell is compressed, the pressure increases continuously. Eventually, at point “B”, the pressure induced infiltration in the largest nanopores is activated and the liquid phase becomes highly compressible. As a result, buckling takes place. As a major wrinkle is formed, the stress quickly drops to “C”. In the NMF cell, because the cell wall is supported by the liquid phase, the buckling can occur only outward, leading to a sudden increase in system volume, ΔV , and thus the cell becomes only partly filled. Under this condition, the system behavior is similar to that of an empty cell, until the cell is compressed to point “D” and ΔV is “consumed” by wrinkle folding. As the liquid phase starts to carry load again, the nominal stress increases from “D” to “E”. When P rises to 32 MPa, the pressure induced infiltration is re-activated, forming the second plateau “EF”. As the plastic strain in cell wall is increasingly large, abrupt cracking occurs at point “F”, somewhat similar with the failure observed in the water-filled cell. The total system volume change associated with the second loading is about 170 mm^3 , smaller than the total nanopore volume; that is, the energy absorption capacity of the nanoporous silica gel is not fully utilized. As the cell becomes empty, the nominal stress drops to 7 MPa, after which the system behavior is similar to that of an empty cell (section “GH”). According to Table A-1, compared with the energy absorption efficiency of an empty cell, U/m of the NMF liquid filled cell is more than 20% larger and U/V is more than two times higher.

In order to gain more insights into the buckling mechanism, finite element (FE) simulations were carried out for both empty and the NFM-liquid-filled steel tubes by using ABAQUS. The geometry, the Young’s modulus (190 GPa), the yield stress (520 MPa), and the strain hardening exponent (0.4) of the tube were the same as that in the experiment. A rigid piston was placed at the top surface with a displacement-controlled motion, and the bottom of the tube was clamped rigidly. To simulate the behavior of the NFM liquid, a phenomenological approach was taken: the tube was first filled with a liquid with the bulk modulus of 2.1 GPa, the same as that of water; upon loading, the pressure of the liquid quickly increased to 18 MPa, at which infiltration and the cell-wall buckling started. Using the pressure-volume curve of the NMF liquid measured earlier, during the numerical simulation, the effective bulk modulus of the liquid filler was adjusted

to decrease as a function of the cell volume. Finally, from both the force and the displacement acting on the piston, the relationship between the nominal stress and strain was computed, as shown in Fig.A-3. It can be seen that the simulation has qualitatively captured the buckling initiation condition of the pressurized cell. The calculated critical nominal stress at the onset of cell-wall buckling is about 40 MPa, in good agreement with the experimental data. In terms of the buckled shape, the NFM liquid filled cell wrinkles and folds outward, and thus the wrinkle pattern is quite regular; whereas the empty cell may fold inward, and the pattern is relatively jerky, fitting well with the experimental observations (Fig.A-4). Note that, prior to the buckling, the extended yielding of tube wall occurs along the radius direction. If this effect were ignored, the calculated buckling stress and wrinkle size would be much larger than the experimental observations. Due to the oversimplification of the boundary conditions and the material properties, the relaxation valley “CD” as well as the second increase in load in Fig.A-2 cannot be simulated.

The energy absorption behavior of the NMF filled steel cell under dynamic loading was analyzed by using the blast simulator in the Powell Labs, UCSD. Two steel cells (height: 2.5”; diameter: 2”; wall thickness: 1/8”) were filled by a NMF liquid that contained 15 g of surface treated MCM41. The details of surface treatment will be discussed below in Section C. The average nanopore size was 2 nm. The cells were filled by saturated potassium chloride solution. They were mounted on a target aluminum alloy plate by using epoxy glue. A projectile, which was an aluminum alloy plate of the same size and weight as the target, was projected at the speed of 20 m/s, as shown in Fig.A-5. The mass of the aluminum alloy plate was 35.5 kg. The kinetic energy of the projectile was 7.1 kJ. The momentum was 712 kg·m/s.

If the impact were perfectly elastic, i.e. if no energy were absorbed, the projectile would stop and the target plate would move at 20 m/s. In the experiment, it was observed that after the impact, the two plates moved at about the same speed; that is, the impact was nearly perfectly plastic; that is, the energy absorption has reached the upper limit. The total kinetic energy of the two plates after the impact was 3.6 kJ. The total output linear momentum of the two plates was 708 kg·m/s. It can be seen that the linear momentum did not vary while the kinetic energy decreased by 49% (the upper limit is 50%). The dissipated energy was 3.5 kJ. That is, the energy absorption efficiency of the MCM41 was more than 100 J/g, much higher than that of any existing energy absorption materials. The high efficiency should be attributed to the nanocapillary effect as well as the internal friction associated with the forced flow of liquid in nanopores.

The impact experiment is still on-going. The amount of MCM41 will be reduced so that the “true” energy absorption efficiency can be measured. The system is being reconstructed so that the upper limit of the speed of projectile can reach 60 m/s. Thus, the energy absorption efficiency can be measured as a function of loading rate in a broad range.

B. Mechanoelectric and Thermoelectric Energy Conversion Associated with Liquid Infiltration

In the calorimetric measurement that will be discussed below, it was noticed that the measured heat generation did not match the absorbed mechanical work. It is thus assumed that the mechanical work can be converted to other forms of energy, such as solid-liquid interfacial tension (the “strain” energy) as well as the electric energy.

As an electrolyte solution contacts an electrified solid surface, their distribution becomes heterogeneous. As a result, a layered structure of solvated ions is formed in the interface zone. The inner layer, which is often referred to as the Stern layer, is of the highest ion density and the lowest ion mobility; in the outer layer, which is also known as the Gouy-Chapman layer, the ion structure is less ordered and the ion mobility is higher. Beyond the boundary of the interface zone, the ion distribution is random and the bulk liquid phase is neutral. As the liquid flows along the solid surface, the equilibrium ion distribution across the relatively immobile inner layer and the relatively mobile diffusive outer layer would be disturbed; thus, a shear plane is formed, resulting in a zeta (ζ) potential. The stream current caused by the net charges in the diffusive layer of a continuous flow in a circular channel can be assessed as $I = \pi d \sigma_0 v_0$, where d is the

channel size, σ_0 is the effective charge density, and v_0 is the flow velocity in the diffusive layer. Consequently, a potential difference, ϕ^* , is developed along the flow direction:

$$\phi^* = \frac{4\sigma_0 v_0 l_0}{d \cdot \xi} \quad (\text{B-1})$$

where l_0 is the channel length and ξ is the liquid conductivity. This electrokinetic phenomenon has been well appreciated in cathode protection, electropolishing, flow control, etc. Once the flow stops, the equilibrium in the inner and outer layers will be reestablished within a few μs .

Recently, stream currents were observed in silicon nanochannels. However, the total electric energy would be rapidly consumed as the ion structure at the channel surfaces exposed to the electrolyte solution reached the steady-state. That is, the energy conversion capacity would eventually vanish even though the flow continues. One way to solve this problem is to increase the conductivity of the nanochannel wall, e.g. by using a nanoporous electrode. It is envisioned that as the liquid electrification takes place simultaneously over the large nanopore surface, significant electric energy can be generated; and as the electrode is grounded, the initial configuration can be restored. Such a system can extract useful electricity from ambient mechanical motions, which are otherwise wasted or harmful, having immediate relevance to developing energy harvesting devices, active damping stages, self-powered sensor networks, among others.

In the current study, a Chand-Eisenmann nanoporous monel was investigated. Monel is a stainless copper-nickel alloy of a low electric resistivity. The nanoporous structure was achieved by sintering pressurized monel nanoparticles. The nanopore size was around 500 nm. The as-received material was in cylinder form, with the diameter of 9.5 mm and the length of 19.1 mm. The total pore surface area of each cylinder was 6.7 m². The mechanoelectric energy conversion system was formed by firmly clamping a nanoporous monel cylinder (the electrode) in a polyethylene pipe, as shown in Fig.B-1. A counter electrode was placed 10-50 mm away from the monel cylinder. A continuous flow of 20 wt.% aqueous solution of sodium chloride was forced through the electrode to the counter electrode using a MasterFlex L/S 7518-10 digital drive. The monel cylinder and the counter electrode were connected by nichrome wires through a 1 M Ω resistor, R_0 , across which the potential difference was measured by a National Instruments 6936E Data Acquisition (DA) board. The nanoporous monel cylinder was connected to the cathode of the DA board, and the counter electrode was connected to the anode of the DA board.

Figure B-2 shows a typical measurement result of the output voltage, ϕ . Initially, the flow rate, Q , was zero. At time t_0 , the digital drive was turned on and the flow rate was suddenly increased to the set point, in this case 3 cm³/min, and maintained at this level for 100 sec. Then, the flow rate was increased gradually to 10 cm³/min. The increment in each step was 1 cm³/min and the step width was 100 sec. Finally, the digital drive was shut down and the flow rate was abruptly decreased to zero. The output voltage was recorded continuously until it decreased to below 0.2 mV, the resolution of the DA board. Similar measurements were performed for similar systems of different electrode distances, l , at various flow rates. The $\phi - Q$ and $\phi - l$ relationships are shown in Fig.B-3.

According to Fig.B-2, as the electrolyte solution starts to flow a significant output voltage is generated. After the digit drive is turned on, the value of ϕ rapidly rises from 0 to about 68 mV in less than 2 sec., and is stabilized at this level as the flow continues. As the flow rate changes, there is no detectable variation in output voltage. After the flow stops, it takes more than 300 sec. for ϕ to decrease to 0. The measured voltage is positive, indicating that the potential of the electrode is higher than that of the counter-electrode.

The observed phenomena are fundamentally different from the predictions of the electrokinetics theory. First, the measured voltage is quite independent of the flow rate, which is more clearly shown in Fig.B-3. As the flow rate increases from 5 to 20 cm³/min, the variation in ϕ is small and random. Second, ϕ is insensitive to the electrode distance, l . Note that l is not an analog to l_0 in Eq.(B-1). In the stream current theory, as liquid moves along a solid surface, the potential difference would rise. In the current study, because

the pore surface is conductive, ϕ is measured between the electrode and the counter electrode. Third, as the flow stops, the decay of output voltage is slow, with the characteristic time close to that of diffusional transport. If the output voltage were directly caused by the ζ -potential, the discharge time should be comparable with the retention time of the solid-liquid interface layer, i.e. the characteristic time that all the ions in the interface zone are replaced by ions from the interior. At room temperature, the retention time is usually at the ps or μ s level, shorter than the measured discharge time by orders of magnitude. Furthermore, due to the relatively high electrolyte concentration, the Debye distance is around a few nm, which is quite small compared with the nanopore size, and thus the stream current should be dominated by the neutral bulk liquid phase.

Figure B-4 shows the output voltage as a function of time when the external resistance, R_0 , was largely reduced to 100 Ω . In an ordinary stream current system, if the resistance between the two electrodes is relatively small, a new equilibrium is established and the potential difference should be zero, since there is no return path for the ion flow as long as no electrochemical reaction takes place. In the nanoporous system, however, a significant transient voltage is detected. At point “A”, the flow started and the voltage rapidly increased to the peak value of $\phi_m = 19.6$ mV. As the flow continued, the voltage decreased gradually, and in about 160 sec. reached zero. At time “B”, the electrode and the counter electrode were disconnected, grounded for less than 0.5 sec., and then reconnected. It can be seen that the energy conversion capacity was fully recovered. The peak of output voltage following “B” is quite similar to that at “A”.

It is clear that, as the liquid flows, the equilibrium of ion structure at the solid-liquid interface is disrupted. The difference between Figs.B-2 and B-4 is caused by the change in external resistance. The output potential difference can be stated as

$$\phi = \Delta\phi - \phi_0 \quad (\text{B-2})$$

where $\Delta\phi$ is the difference between the potential differences across solid-liquid surfaces at the electrode and the counter electrode, and ϕ_0 is the potential difference in the liquid phase. Initially, when the liquid is at rest, both $\Delta\phi$ and ϕ_0 are zero, so is ϕ . When the liquid starts to flow, the ion distributions at the surfaces of the electrode and the counter electrode become different, which can be attributed to the confinement effect of pore walls as well as the difference in effective flow rate in nanopores and in bulk liquid phase. As the effective ion densities at the solid-liquid surfaces vary, the counter charge densities in the solid phases are different. Consequently, a significant $\Delta\phi$ is developed. When R_0 is large, the current between the electrode and the counter electrode is negligible, and the difference in charge density can be maintained constant; thus, $\Delta\phi$ does not vary with time. In the liquid phase, ϕ_0 is actually dominated by the stream current effect along the polyethylene pipe, which is negligible, primarily because that the Debye distance is much smaller than the pipe diameter and the counter electrode is immersed in the central part of the bulk liquid phase. Hence, the output voltage is actually dominated by the surface polarization effect, independent of the electrode distance and having a long characteristic discharge time associated with ion diffusion processes.

When R_0 is relatively small, the excess surface charges would move from the low-potential end to the high-potential one, forming the measured transient current before the new steady state among the electrode, the counter electrode, and the liquid phase is established. The total charge associated with the transient current is around 15 mC, and the associated electric energy is about 0.2 mJ. Since the total surface area of the nanoporous electrode is 6.7 m², the density of the excess counter charges is 2.2 mC/m², or 1.4×10^{16} e/m², where “e” indicates electron charge. In the 20 wt.% sodium chloride solution, the average cation density is 2.04×10^{27} e/m³, and in a surface layer which is a few nm thick the cation density is at the level of $10^{19} - 10^{20}$ e/m². That is, as the liquid flows, the variation in surface ion density, which is equal to the counter charge density in the solid phase, is around 0.01% to 0.1%. Note that in the parameter range of the current study, the charge density change is quite insensitive to the flow rate, probably because that for the thin interface layer even the lowest flow rate, which is 3 cm³/min. or about 700 μ m/sec., is still quite large and thus the

disturbance effect has been saturated. The factor of liquid motion comes in by affecting the ion distribution in the Gouy-Chapman layer, which in turn influences the Stern layer. The shear motion between the two layers may lead to additional variation in effective surface charge density.

Once the transient current vanishes, the energy conversion capacity of the system is lost. However, as shown in Fig.B-4, at time “B”, as the electrode and the counter electrode were disconnected and reconnected, the energy conversion cycle could be repeated. Clearly, during the grounding process, the system configuration rapidly returns to its initial state and the accumulated excess charges could form the transient current again, indicating that the transient current is directly related to the motions of counter charges in the solid phase, rather than the ion motions in the liquid phase. When the disconnection-reconnection procedures are repeated, electric energy can be generated semi-continuously.

C. Controlling Infiltration Pressure via Surface Treatment

In a previous study, it was confirmed that using chemical admixtures can either increase or decrease the infiltration pressure. However, the addition of admixtures would cause heterogeneous liquid structures, making it difficult to develop reliable systems, especially when the system must work in a broad temperature range. Therefore, it is desirable to directly control the pore surface structure using surface treatment methods. Compared with ordinary surface treatment, the modification of properties of inner nanopore walls is relatively difficult due to the poor surface accessibility. The molecular size of the functional agents must be much smaller than the nanopores, and the diffusion process might take a long time. On the other hand, one advantage of NEAS is that leaching is not a concern. Since many protection systems, such as car bumpers and body armors, work only under the first loading, even if the functional groups are deactivated as a high pressure is applied, it would not affect the energy absorption performance.

In order to validate the above considerations, a Davisil-236845 nanoporous silica gel was investigated experimentally. The average pore size was 16.2 nm; the specific pore volume was 1.07 cm³/g; and the specific surface area was 305 m²/g. The as-received material was in powder form, with the particle size around 250 μm. The surface treatment was performed in a 100-mL round bottom flask, based on the technique discussed by Lim and Stein.⁷ Prior to the treatment, the silica gel was vacuum dried at 100 °C for 24 h. Immediately after the flask was taken out of the oven, a glass topper was used to seal it. Then, 40 mL of Sigma-244511 dry toluene was injected into the flask. While the solution was stirred gently, 1.0 mL of Fluka-92360 chlorotrimethylsilane was injected. The light yellow mixture was stirred for 10 min at ambient temperature, and then refluxed in a hot mantle at 90 °C. The treatment time was in the range of 1–48 h. A drying tube was attached to the reflux apparatus to minimize the influence of moisture. The silica gel was vacuum filtered and washed by dry toluene, and then vacuum dried at 100 °C for 24 h to remove the residual chlorotrimethylsilane. Finally, the sample was washed by distilled water so as to hydrolyze remaining chloride groups and dried again in a vacuum oven.

A stainless steel cylinder was sealed by a steel piston with reinforced gasket, which contained 0.5 g of surface treated silica gel and 7 g of distilled water. The piston was compressed by a type 5583 Instron machine at a constant rate of 0.5 mm/min into the cylinder, applying a quasi-hydrostatic pressure on the liquid phase. When the pressure exceeded 50 MPa, the piston was moved out at the same speed. The loading-unloading cycles were repeated for a few times. The measured sorption isotherm curves of the first cycle were shown in Figure C-1. The curves of the second cycle were shown in Figure C-2. The sorption isotherm curves in the following cycles were nearly identical to the second ones. The specific system volume change was defined as the intrusion volume of the piston divided by the mass of silica gel.

Figure C-1 indicates clearly that the surface treatment is quite successfully. Without any treatment, the nanopore wall is hydrophilic. Thus, when the silica gel is immersed in water, at the ambient pressure water molecules enter the nanopores spontaneously. As the nanoporous space is filled, further increase in pressure would lead to only a negligible increase in water molecule density in the nanopores, since water is quite

incompressible. Thus, no infiltration could be measured. As the silica is surface treated, chlorotrimethylsilane molecules diffuse into the nanopores and form a hydrophobic layer of $\text{OSi}(\text{CH}_3)_3$ groups through a condensation reaction with OH^- groups. As the treatment time increases, more and more silane groups attach to nanopore wall and surface coverage, c , keeps increasing. Eventually, nanopore surface transfers from wettable to non-wettable. Under this condition, water molecules cannot enter the nanopores spontaneously. A pressure must be applied so that the capillary effect can be overcome. In the current study, the infiltration pressure, p_{in} , is defined as the pressure at the onset of infiltration, which is dominated by the behaviors of water molecules in the largest nanopores. As p_{in} is reached, water molecules are compressed into the nanoporous space, resulting in the formation of infiltration plateau in sorption isotherm curve. Due to the pore size distribution, the infiltration plateau is of a finite slope. When most of the nanopores are filled, the system compressibility is lost and the sorption isotherm curve becomes stiff. Upon unloading, due to the difficulties in gas phase nucleation and growth, the defiltration is much less pronounced compared with the infiltration. That is, the confined liquid tends to remain in the nanoporous silica gel at reduced pressure, even though it is nominally energetically unfavorable. Consequently, the excess solid-liquid interfacial energy cannot be released, which is the mechanism of energy absorption. Figure C-1 shows clearly that as the treatment time, t_{T} , is longer than 1 h, the pore surface becomes hydrophobic. As t_{T} increases to 48 h, p_{in} rises to about 8 MPa. Further increase in t_{T} would not cause pronounced variation in p_{in} , indicating that the surface coverage has been saturated.

The infiltration volume, which can be taken as the width of the infiltration plateau, is about $0.83 \text{ cm}^3/\text{g}$, smaller than the gas absorption measurement result, probably because of the reduction in accessible nanopore volume caused by infiltration of silane chains as well as the inaccessibility of smallest nanopores. It decreases slightly as the treatment time increases, which is in agreement with the increase in silane group density. However, the variation in infiltration volume is only secondary compared with the treatment time effect on the infiltration pressure. Thus, the change in energy absorption efficiency, which can be measured by the area enclosed by the loading-unloading loop, is nearly proportional to p_{in} .

Note that the $p_{\text{in}} - t_{\text{s}}$ relationship is highly nonlinear. As the critical treatment time is reached, initially the infiltration pressure increases rapidly with a small increment of t_{T} . The t_{T} sensitivity of infiltration pressure decreases as t_{T} rises. When $t_{\text{T}} > 48 \text{ h}$, the surface group density is saturated and further increase in t_{T} does not cause detectable change in p_{in} . The nonlinearity of $p_{\text{in}} - t_{\text{s}}$ relationship should be attributed to that, as the surface coverage is relatively low, the silane groups attached on the nanopore surface are far and few between, and therefore they are relatively independent of each other. As the silane group density becomes increasingly high, it is more and more difficult for chlorotrimethylsilane molecules to access untreated silica surface, and thus the increase in surface group density becomes slower.

After the first loading, since most of the porous space is occupied, at the second loading the infiltration volume is much smaller. From Figure C-2, it can be seen that the sorption isotherm curves at the second loading are almost identical for all the samples, regardless of the large variation in surface treatment time. The limited infiltration occurs at relatively low pressure, nearly the same as the defiltration section of the sorption isotherm curve at the first loading. That is, while in most of the porous space the defiltration is difficult, there exists a reversible part of confined liquid, likely in the smallest accessible nanopores since the defiltration driven force is inversely proportional to the pore size. Since the specific energy involved in this process is much smaller than that in the first loading cycle, it does not have pronounced influence on the energy absorption performance. Moreover, since even when the silica gel is surface treated for 48 h the defiltration is still difficult, the uniformity of surface groups should not be a vital factor governing the defiltration behaviors.

D. Developing Energy Absorption Systems Using Carbon Materials

One drawback of the previously discussed systems is the complicity in preparation of the nanoporous silica gel, which consists of sophisticated template formation, activation, and surface treatment steps.

Moreover, compared with many other nanoporous materials, the surface area of the silica gel is relatively low, leaving a considerable room for improvement. In view of these considerations, we investigate a nanoporous carbon. Nanoporous carbon is probably one of the earliest nanoporous materials used by human being. The nanoporous structure is formed by the imperfect packing and bending of graphene nanolayers. Usually, they are synthesized by appropriate carburization treatment of organic materials, while a few deposition or nanocasting techniques have also been developed. Nanoporous carbons are of pore sizes typically lower than 2 nm, and pore surfaces of about 1000 m²/g, much larger than that of nanoporous silica gels. They are easy to synthesize, cost efficient, and available in large volumes, ideal for developing large-scale dampers.

The testing sample was produced by mixing 0.5 g of J. T. Baker E345-07 nanoporous carbon in 8.0 g of liquid phase. The as-received carbon was in powder form, with the particle size of about 20 μm and the specific surface area of 800 m²/g. The liquid phase was chosen as Fluka 95682 *p*-Xylene, a nonpolar chemical with the molecular formula of C₆H₄(CH₃)₂ and the molecular weight of 106.17. Under ambient condition, the nanoporous carbon was non-wettable to *p*-Xylene, and thus the liquid cannot be absorbed into the nanopores spontaneously.

The carbon-*p*-Xylene mixture was sealed in a steel cylinder. Using a type 5569 Instron machine, a hydrostatic pressure, *p*, was applied on the liquid phase through the steel piston. The pressure was increased by moving the piston into the cylinder at a constant rate of 1 mm/min. The effective strain rate was at the level of 10⁻³/sec, and thus the loading condition was quasi-static. Two sets of experiments of different maximum pressures were performed. In the low-pressure experiment, as the pressure exceeded 55 MPa, the piston was moved back at the same rate until the pressure was reduced to zero. In the high-pressure experiment, the pressure was increased to 155 MPa, followed by the unloading. In both sets of experiments, the loading-unloading process was repeated for more than six cycles. The measured sorption isotherm curves are shown in Figs.D-1 and D-2.

Through Fig.D-1, it can be seen that the nanoporous carbon works quite well under the cyclic loading. In the first loading-unloading cycle, as shown by the dashed line, the sorption isotherm curve is initially quite linear, indicating that *p*-Xylene cannot enter the nanopores if the pressure is relatively low. When the pressure reaches 41 MPa, the capillary effect of the largest nanopores is overcome and the liquid begins to infiltrate into the nanoporous particles. As the pressure increases, more and more smaller nanopores are involved in the pressure induced infiltration, and consequently an infiltration plateau is formed. The profile of the infiltration plateau is relatively linear, suggesting that the nanopore size distribution of the nanoporous carbon is parabolic.

In the experiment discussed above the nanopore volume of the nanoporous carbon is not fully utilized, since the maximum pressure is only about 55 MPa, insufficient to overcome the capillary effect of the smallest nanopores. If the maximum pressure is increased to 155 MPa, as shown in Fig.3, the width of the infiltration plateau increases considerably, indicating that most of the nanopores, including those not involved in the low-pressure infiltration, are intruded by the liquid. The profile of the first-cycle sorption isotherm curve is somewhat similar to that of Fig.2, while the infiltration plateau width is 1.25 cm³/g, close to the total nanopore volume, leading to an improved energy absorption efficiency of 49 J/g.

From Fig.D-2, it can be seen that under a high pressure the nanoporous structure is damaged during the high-pressure infiltration process. The decreases in accessible pore volume indicates that the nanopores collapse, and the decrease in infiltration pressure suggests that the collapsed nanopores are those of smallest sizes, which is in agreement with the fact the capillary pressure increases as the pore size decreases. The occasional increase in accessible pore volume indicates that nanopore reopen can also take place, which should be caused by the change in packing mode of graphene nanolayers. Particularly, as the porosity decreases to a certain level, the close-packed graphene nanolayers can be relatively unstable and therefore they can break down into nanoporous structures as a high external pressure are applied. However, such an additional porosity process is unrepeatable, and thus should be regarded as a random factor. Under this condition, after the first loading-unloading cycle, the energy absorption efficiency of the system is not only

smaller but also unreliable. Hence, for the design of protective devices, only the first loading should be taken into consideration, and the system is suitable only for one-time uses.

In addition, similar energy absorption behaviors have been observed for carbon nanotubes and other types of carbon-liquid systems, indicating that nanoporous carbon (including carbon nanotubes) are suitable candidates for the solid phase in nanoporous materials functionalized liquids.

E. Dependence of Infiltration and Defiltration Properties on Liquid Composition

The influence of liquid composition on infiltration and defiltration was analyzed systematically. We first investigated a system based on sodium chloride solution. It is known that the addition of aqueous electrolytes such as NaCl can increase the surface/interfacial tension, and thus would have a beneficial effect on the energy absorption efficiency. Furthermore, the NaCl admixture can serve as an anti-freezing agent such that the system can be used at temperatures lower than 0°C. Since the change in pH value is negligible as the NaCl concentration, c , varies, the acid and base terms, γ^+ and γ^- , in the van Oss-Chaudhury-Good (VCG) equation are quite constant. As a result, at macroscopic level, the relationship between the interfacial energy and the NaCl content is nearly linear.

A mixture of the silica particles and the NaCl solution was sealed in a steel container. By using a type-5569 Instron machine in displacement control mode, the system was compressed through a sliding steel piston at a constant rate of 1.0 mm/min. The friction force between the piston and the container was in the range of 20-30 N, which was negligible compared with the peak loading. When the applied pressure exceeded 50 MPa, the crosshead was stopped and then moved back at the same rate of 1.0 mm/min. The amount of the mesoporous silica particles used in each test was 0.5 g.

Altogether, 8 systems of different NaCl concentrations were studied. For each system, 4-7 samples were tested. The typical sorption isotherm curves are shown in Fig.E-1. The specific volume change is defined as the ratio of the system volume change to the amount of mesoporous particles. The areas between the loading and unloading curves indicate the specific absorbed energy, E^* , which is shown in Fig.E-2 as a function of c . The inflow pressure, P_{in} , is taken as the pressure at the center point of the plateau region of the loading curve (see Fig.E-3), which will be discussed in detail shortly. The liquid-silica interfacial energy can be estimated through $\Delta\gamma = p_{in}\bar{r}/2$, and the result is also shown in Fig.E-3.

As the NaCl concentration increases, the system stiffness becomes higher. When c is changed from 0 to 30wt.%, the effective bulk modulus rises by about 20%. This is in consistent with the literature data of the bulk moduli of NaCl solutions. The specific volume change associated with the plateau region, however, remains the same, as it should, since it reflects the pore volume fraction. The value of the inflow pressure, p_{in} , increases with c , i.e. with the addition of the NaCl, the inflow is more difficult, which should be attributed to the increase in $\Delta\gamma$.

As shown in Fig.E-3, unlike that in the macroscopic cases where the surface energy varies linearly in a broad range of NaCl concentration, for the mesoporous silica the $\Delta\gamma$ - c relationship is quite nonlinear. When $c > 20$ wt.%, the nonlinearity may be related to the saturation effect. When c is lower than 5 wt.%, the nonlinear behavior cannot be captured by the conventional interfacial energy theories, which are usually based on the calculations of the change in chemical potentials associated with the ion distribution in the interfacial zone. In the nanopores, the confinement effect of the pore walls must be taken into account. Since the pore radius is comparable with or even smaller than the interfacial zone, there does not exist a “bulk liquid” phase, and thus the molecular interaction can be significantly affected. However, currently there is still no satisfactory model that can capture the details of this size effect.

Comparison between Fig.E-2 and Fig.E-3 shows that, while both E^* and p_{in} increase with c , the former is less sensitive to c . As the NaCl concentration increases from 0 to 23.1wt.%, p_{in} increases by about 30% and E^* increases by only about 15%. This is because that when p_{in} increases, p_{out} , the critical pressure at which the outflow starts to occur, also rises (see Fig.E-1), and therefore the beneficial effect of increasing p_{in} on E^* is

lowered. Thus, the mechanisms how the NaCl concentration affects the inflow and outflow processes must be different. The inflow can be discussed in the framework of surface flow processes, in which the dominant factor is the balance of the surface and interface forces. The outflow, on the other hand, may be considered as an equilibrium phase transformation, for which the key factors are still under investigation.

If the molecular size of the chemical admixture is larger, comparable with the nanopore size, the confinement effect of pore walls can be pronounced. We tested a system containing 0.5 g of Fluka 100 C₈ reversed phase end-capped mesoporous silica gel and immersed in 7 g of aqueous solution of Sigma C6445 sodium cholate hydrate (SCH) and sigma C3125 ammonium 8-anilino-1-naphthalenesulfonate (1,8-ANS-NH₄). Figure E-4 shows the sorption isotherm curves of systems containing no SCH. The zero 1,8-ANS-NH₄ concentration curve indicates the behavior of the system based on pure water. With the addition of 1,8-ANS-NH₄, since the promoter can “carry” water molecules into the nanopores, the required infiltration pressure to overcome the capillary effect is lowered considerably. Due to the relatively large molecular size, it is more difficult for the 1,8-ANS-NH₄ molecules to enter into smaller nanopores than into larger nanopores. Thus, the extent of decrease in infiltration pressure is higher in the larger nanopore region. This phenomenon becomes more significant as the 1,8-ANS-NH₄ concentration is increasingly high. When the 1,8-ANS-NH₄ concentration increases to 3.0 wt.%, the infiltration plateau is obviously two staged. The low-pressure section, which will be referred to as stage I (“a”) in the following discussion, is associated with the relatively large nanopores in which the 1,8-ANS-NH₄ infiltration is easy. The high-pressure section, which will be referred to as stage II (“b”) in the following discussion, is related to the small nanopores. The width of the stage-I infiltration plateau indicates the specific volume of large nanopores, which is around 0.15 cm³/g, about 30% of the total pore volume. The similar two-staged infiltration behavior can be obtained by adding 1.5 wt.% CSH, as shown by the zero 1,8-ANS-NH₄ concentration curve in Fig.E-5. However, the width of stage-I infiltration plateau is only about 0.08 cm³/g, much smaller than that of 1.5 wt.% 1,8-ANS-NH₄, suggesting that it is more difficult for the CSH molecules to infiltrate into the mesoporous silica gel. This is in consistent with the fact that the molecular size of CSH is larger than that of 1,8-ANS-NH₄. Since the area of the silica surface exposed to the liquid phase is very large and it is difficult to form micelles in the nanopores, the critical micelle concentration (CMC) is quite high, which is in agreement with the experimental observation that the infiltration pressure changes somewhat continuously as the promoter concentration increases.

With the addition of 1.5 wt.% 1,8-ANS-NH₄, it can be seen that the infiltration plateau becomes three-staged. The three stages will be referred to as stage I (“a”), stage II (“b”), and stage III (“c”), respectively. The width of stage I is similar to that of the curve of zero 1,8-ANS-NH₄ concentration, while the infiltration pressure is lower. The total width of stages I and II is close to that of stage I of the 1.5 wt.% 1,8-ANS-NH₄ concentration curve in Fig.E-4. Clearly, the transition from stage I to stage II is caused by SCH, and the transition from stage II to stage III is caused by 1,8-ANS-NH₄. The three-staged sorption isotherm curve can be somewhat regarded as the superposition of the sorption isotherm curve of the system containing only SCH and the sorption isotherm curve of the system containing only 1,8-ANS-NH₄. As the SCH or 1,8-ANS-NH₄ concentration increases to 3.0 wt% (see Fig.E-6), however, the simple superposition principle breaks down. Under this condition, the sorption isotherm curve is two staged again; that is, the SCH molecules and the 1,8-ANS-NH₄ molecules are no longer independent of each other. Rather, they enter the nanopores as a unified system. The width of stage I is larger than either that of SCH or that of 1,8-ANS-NH₄, i.e. as the promoter concentration is relatively high, they promote the infiltration of each other.

Chemical admixtures may suppress defiltration. Two types of admixtures were investigated. One was Sigma U5378 carbamide, with the molecular formula of NH₂CONH₂, the molecular weight of 60.06, and the molecular size of about 0.3 nm; and the other was Sigma D1685 sodium bis(2-ethylhexyl) sulfosuccinate (SBS), with the molecular formula of C₂₀H₃₇NaO₇S, the molecular weight of 444.56, and the molecular size of about 2 nm. Both of them are surfactants that can be dissolved easily in water. As carbamide is added in water, with the two polar amino groups in its molecular, molecular clusters of gas and liquid species can be formed more easily by hydrogen bonds, and therefore the gas solubility increases. SBS is a long chain

molecular, with the chain length comparable with the nanopore size. With the two ethyl groups on both side of the chain, it can block the nanopore.

After adding the admixtures in 7g of distilled water, the liquid was mixed with 0.5 g of Fluka 100 C₈ reversed phase end-capped silica gel and placed in a steel cylinder. The silica gel was degassed at 150 °C for 12h in the vacuum oven. Addition of 10 wt.% of carbamide has little influence on the infiltration pressure, $p_{in} = 15.6$ MPa, and the infiltration volume, $V_{in} = 0.47$ cm³/g, compared with the pure water based system ($p_{in} = 16.0$ MPa and $V_{in} = 0.45$ cm³/g). The sorption isotherm curves of the first loading-unloading cycles of the carbamide modified system and the pure water based system are almost identical, except that for the carbamide modified system p_{in} is slightly lower by about 0.5 %, within the uncertainty range of the pressure measurement machine. The value of V_{in} is 0.47 cm³/g, slightly smaller than the gas absorption measurement result of the specific nanopore volume. Compared with the “ideal” curve, the slope of the infiltration plateau of the experimental data is finite, which should be attributed to the nanopore size distribution. Since the capillary effect in larger nanopores is easier to overcome, the infiltration begins in the largest nanopores. As the pressure increases, smaller nanopores are filled, and eventually at 28 MPa the infiltration is nearly complete. As the pressure is lowered, defiltration begins at 3.2 MPa. Note that the measured defiltration plateau is also of a finite slope, which, again, should be related to the pore size distribution. That is, defiltration in smaller nanopores is easier than in larger nanopores, since the capillary “driving force” of liquid motion is higher and the energy barrier of gas phase nucleation is lower.

A remarkable phenomenon is that, although the most dominant characteristic of this system, the solid-liquid interfacial tension, is insensitive to the addition of carbamide, the defiltration volume, which can be estimated as the second-cycle infiltration plateau width $V_d = 0.04$ cm³/g, is largely reduced by about 67 % compared with the defiltration volume $V_d = 0.12$ cm³/g of the pure water based system. It can be seen that the second-cycle infiltration pressure is much higher than that in the first cycle, close to the high-pressure section of the first-cycle infiltration plateau, suggesting that the reversible part of confined liquid is in the smallest nanopores. With the addition of carbamide, since p_{in} does not vary much, the “driving force” of defiltration caused by the capillary effect of the lyophobic nanopore surface remains the same. Thus, the decrease in defiltration volume should be associated with the increase in gas solubility. The two amino groups in the carbamide molecule can promote the formation of molecular clusters of gas and liquid species, and therefore more gas molecules can be dissolved in the carbamide modified liquid phase. It is assumed that as a “structure breaker”, carbamide disrupts the structure of water by setting up new hydrogen bonds when a cavity is produced to accommodate the solute. As a result, in a nanopore, the energy barrier of gas phase nucleation increases, and even under a relatively low pressure the confined liquid does not come out.

As the carbamide concentration is increased to 20 wt.%, while V_{in} shows no significant change, the decreases in $p_{in} = 14.0$ MPa and $V_d = 0.02$ cm³/g become more pronounced. The change in V_d is 83 % compared with $V_d = 0.12$ cm³/g of the pure water based system. The variation in p_{in} , while still secondary compared with the change in V_d , is about 12.5 % compared with $p_{in} = 16.0$ MPa of the pure water based system, leading to a lower capillary “driving force” of defiltration. The defiltration volume, V_d , is almost zero. In such a NEAS, the energy absorption is complete and no liquid would be “bounced back” after the first unloading.

When the system is modified by 2% SBS, unlike the carbamide modified system, the infiltration volume $V_{in} = 0.39$ cm³/g is smaller than that of the pure water based system by about 13.3 %. Moreover, the infiltration pressure, $p_{in} = 15.0$ MPa, is reduced by 6.3 % compared with the pure water based system, especially at the beginning section of infiltration plateau. That is, in the relatively large nanopores the infiltration can be promoted by the SBS molecules, since they are effectively wetting to the nanopore surfaces. In the relatively small nanopores, the promotion effect on infiltration is less pronounced. Particularly, in the smallest nanopores associated with the high-pressure end of the infiltration plateau, the infiltration cannot take place, resulting in the reduced V_{in} . According to previous experimental data and molecular dynamics

simulations, the admixture molecule demands a free volume several times larger than itself to enter a nanochannel; otherwise the repelling effect, even for nominally wettable nanochannel walls, would be dominant.

F. Developing Solid-Like Energy Absorption Systems

If the molecular size of the admixture is even larger (e.g. by adding polyelectrolyte the macromolecules can crosslink together and form a network), the liquid viscosity can increase significantly and eventually the system becomes solid-like. However, the energy absorption performance is not affected much. This has been confirmed by using poly(isobutylene-co-maleic acid) sodium salt (PIMA-Na), as shown in Fig.F-1.

For the infiltration process, the free energies of the two states of the liquid confined in gel network (state 1) and the liquid confined in a nanopore (state 2) can be related through

$$\xi_2 = \xi_1 + PV - \gamma A - \Delta\mu \cdot V + P^2V / 2K \quad (F-1)$$

where ξ_1 and ξ_2 are the free energies of state 1 and state 2, respectively; P is the applied pressure, V is the volume of the water; γ is the excess solid-liquid interfacial tension; A is the associate solid-liquid interface area; $\Delta\mu$ is the specific free energy difference; and K is the bulk modulus of the gel, which is around 0.1 GPa.¹² The 2nd, 3rd, 4th, and 5th terms at the RHS of Eq.(F-1) capture the external work, the solid-liquid interaction, the confinement effect of the PIMA-Na gel, and the strain energy, respectively. As the first order approximation, V can be estimated as $\pi \cdot r^2 d$, with r being the pore radius and d the effective depth of the water column in the nanopore. Similarly, $A = 2\pi \cdot r \cdot d$.

At equilibrium, $\xi_2 = \xi_1$, and thus

$$P = \frac{2\gamma}{r} + \Delta\mu - \frac{P^2}{2K} \quad (F-2)$$

For the pure water based system, since the liquid matrix is nearly incompressible and free, the last two terms in Eq.(F-2) are negligible. Hence, since the change in γ caused by the sodium ions is small, the difference in infiltration pressure between the PIMA-Na modified system and the pure water based system is

$$\delta P = \Delta\mu - \frac{P^2}{2K} \quad (F-3)$$

The total nanopore volume of the system in the current study is 0.26 cm³. At this volume variation level, according to the testing data of pressurized polyelectrolyte gels, $\Delta\mu$ is a few kPa. Consequently, when $P = 17$ MPa, $\delta P \approx -1.4$ MPa, which looks quite plausible.

G. Computer Simulation of Liquid Behaviors in Nanopores

The fundamental infiltration and defiltration mechanisms of nanofluidics are distinct from that of bulk phases, as analyzed by a number of molecular dynamics (MD) simulations in the past a few years. However, in most of these analyses, the liquid molecules were placed in vacuum nanotubes or nanochannels. In a bulk liquid, the gas nanophase that typically consists of a few to several hundreds of gas molecules often has secondary influence on the liquid motion, in part due to the low gas molecule density that is usually a few orders of magnitude smaller than that of liquids. Thus, within a constant volume, the overall forces exerted on liquid by gas molecules are negligible, compared with liquid-liquid and liquid-solid interactions. In a nanochannel, however, due to the radial confinement the effective gas molecular density significantly increases. As the nanotube diameter is smaller than a few nanometers, a single gas molecule could “block” the nanotube such that the infiltrated liquid molecules could not easily bypass it. In our recent experimental study on nanoporous silica gels, as will be discussed in detail shortly, it was discovered that the liquid defiltration in

nanopores of relatively high gas concentrations was much easier than in nanopores of relatively low gas concentrations.

CNTs with varying radii are employed as model nanoenvironments to explore the fundamental size effects of nanofluidic behaviors, without introducing additional parameters such as the pore surface features. Insights of effective gas solubility was obtained by studying a cluster of 12 carbon dioxide (CO_2) molecules in water confined by CNTs of four different radii. The CO_2 cluster was placed in the middle of a long open-ended tube and surrounded by water molecules, and the MD simulations were carried out at a constant temperature (300 K) with a constant pressure of 10 MPa for 20ps, by using a condensed-phased optimized molecular potential for atomistic simulation studies (COMPASS). The averaged distance between carbon atoms in the nearest CO_2 molecules is plotted as a function of CNT radius in Fig. G-1, where the separation is considerably larger in larger tubes, indicating an easier solvation. In a small nanotube (e.g. (10,10)), the space is insufficient for the water molecules to surround and dissolve the CO_2 molecules, and thus the integrity of the CO_2 cluster remains; whereas in a relatively large pore (e.g. (40,40)), the CO_2 molecules were quickly dissolved in the water in a few ps. That is, there is a critical pore size below which the solvation of CO_2 molecules becomes difficult. The observations hold at other pressures; thus, during the liquid infiltration into a small nanochannel with increasing pressure, the CO_2 cluster is likely to remain with high pressure and thus play an important role, whereas the CO_2 phase can be rapidly dissolved in a large tube and the solid-liquid interaction dominates the nanofluidic behavior. Note that, if the gas molecules cannot be entrapped, such as at a large solid surface or in a through fluidic channel, the gas solubility would exhibit different characteristics as the length scale approaches to the nanometer level. Moreover, in the current study, the simulation time is insufficient to reveal the saturated liquid-gas mixture configurations, which have been discussed by a number of researchers.

Inspired by the size effect of gas solubility study, (10,10) and (40,40) CNTs were investigated to analyze the effect of gas phase on liquid infiltration-defiltration behaviors in nanoenvironment. One end of the CNT was closed, providing a simplified boundary condition for either the end of a closed nanochannel or the symmetric compression of liquid and “gas phases” (CO_2 molecules) from both ends of a long nanochannel. Initially, the tube either was vacuum or contained a certain number of CO_2 molecules, and its surface was assumed smooth. The CNT length was chosen such that the end effect is negligible in the initial infiltration stage (but it will become important at the final stage of infiltration and the initial stage of defiltration, when the entire pore is almost filled with water, discussed below). Depending on the tube size, the CNT was surrounded by several thousands of water molecules at a constant temperature (300 K) with an initial pressure of 0.1 MPa. By varying the size of the computational cell, the pressure variation in the system (up to 100MPa in this study) was obtained through the bulk modulus of water (2.1 GPa). All pressure values referred in this study are that in the water phase. At any pressure, a normalized volume fraction of the infiltrated water molecules was calculated, which is defined as the number of H_2O molecules in the CNT divided by that at 100 MPa, both measured at 50 ps after quasi-equilibrium. In essence, the volume fraction indicates the infiltrated volume of liquid in the nanotube at a given pressure.

In a bulk water structure, a H_2O molecule has four hydrogen bonds; however, a molecule adjacent to the open end of a carbon nanotube (CNT) tends to lose two hydrogen bonds, thus having a higher energy level. Therefore, in absence of other assistances (e.g. an external pressure), the H_2O molecules near the CNT open end must rely on random thermal vibrations to overcome the energy barrier to lose hydrogen bonds and to infiltrate into the hydrophobic CNT. When a (10,10) CNT was initially vacant, with the aid of pressure difference (at 78 MPa), H_2O molecules gradually diffused into the CNT and the normalized water volume was about 27% (Fig. G-2a). On the other hand, when the same CNT initially contained a single CO_2 molecule, due to the van der Waals attraction exerted by the CO_2 molecule, under the same pressure the normalized water volume was 68% (Fig. G-2b), nearly 2.5 times larger. The effect of CO_2 molecule on infiltration is obvious where the CO_2 molecule has helped the liquid to enter the nanotube. Note that in most of previous MD studies

on liquid motions in nanochannels, this important effect was ignored, which would lead to an underestimation of the liquid infiltration rate.

The CO₂ molecules can also be critical to the defiltration process. In the MD simulation, a long one-end-capped (10,10) CNT which encompassed 10 CO₂ molecules was analyzed. Due to the dramatically decreased gas solubility in a small nanopore, when the pressure was increased, the infiltrated H₂O molecules pushed the CO₂ molecules toward the capped end to form a cluster (similar to the insert in Fig. 1); meanwhile, the water pressure was increased continuously, leading to the entrance of more H₂O molecules, which stabilizes at 100 MPa (Fig. G-3).

By comparing the total free energies of a CNT filled by water molecules and an empty CNT with the same amount of water molecules surrounding it, the effective excess CNT-water interfacial tension can be obtained as 58 mJ/m². According to the classic capillary theory, the infiltration pressure should be around 160 MPa, qualitatively fitting with the MD simulation result, indicating that the long-term structure of the ensemble is governed by thermodynamics. This was recently confirmed by continuum analyses, mean-field models and simulations of nanofluidic properties, as well as atomic simulations on saturated gas concentrations, where unique nm-scale phase behaviors were revealed. However, since thermodynamic models predicted reversible system performance, in order to capture the hysteresis of infiltration-defiltration loop, kinetics of liquid-gas-solid interaction must be taken into consideration. In the current study, it was observed that upon unloading the water molecules were confined in the CNT until the pressure was lower than about 25 MPa, at which the H₂O molecules began to “flow” out. In essence, at the defiltration pressure of 23 MPa in this simulation, the gas molecule cluster was able to repel the water molecules out. About 1/3 of the water molecules exited the nanochannel when the pressure was reduced to 1 bar. Note that a prerequisite for the formation of gas molecule cluster is that the CNT diameter should be sufficiently small, less than a few nanometers.¹⁵ Thus, the numerical analyses indicated that the defiltration is possible for relatively small nanopores and the trapped gas phase is the critical driving force, both in qualitative agreement with the experimental observations that will be discussed below.

By contrast, if the nanopore was relatively large, with an increasing pressure the water molecules infiltrated into the nanopore and dissolved the CO₂ molecules (insert in Fig. G-1), and thereby fulfilled the CNT volume at a sufficiently high pressure. The situation then became similar to that of Fig. G-2a where the CNT was initially vacant and the liquid-solid interaction dominates. To study the effect of CO₂ molecules on the liquid defiltration, in Fig. G-3 MD simulations for the same (10,10) CNT without and with CO₂ molecules were compared. In absence of the CO₂ molecules, the normalized infiltrated water volume was about 27%; the number of the H₂O molecules inside the CNT remained constant until the pressure was increased to a critical value, at which pressure-induced infiltration started to take place. The higher pressure lifted the system energy to the threshold of breaking roughly one-half of the hydrogen bonds for several H₂O molecules close to the tube opening. Subsequently, more H₂O molecules could enter the CNT and the infiltration took place when the pressure was between 78MPa and 100MPa (saturation). The infiltration pressure was thus determined as about 80 MPa. Upon removing the external pressure, all of the H₂O molecules were “locked” inside the CNT, since, after the H₂O entered into the CNT, new hydrogen bonds were generated and the H₂O molecules had a more favorable energy level. In addition, a van der Waals attraction existed between the CNT wall and the infiltrated H₂O molecules. Thus, the numerical simulation predicted that “non-outflow” is possible for either small nanopores without gas molecules trapped inside or large nanopores where the gas phases were dissolved in water.

In order to validate the MD simulation results of the gas phase effect on nanofluidic behaviors, a pressure-induced-infiltration experiment was performed on a hydrophobic nanoporous Fluka C₈ end-capped reversed phase silica gel of the average pore size of $r = 7.8$ nm and the standard deviation of 2.4 nm. At the first-order approximation level where the solid-liquid interaction was characterized by a single parameter of the effective interface tension, it could be employed as an “analog” to the CNTs, even though the details of its pore surface features were abundantly different. The specific surface area of the silica gel was 287 m²/g and

the particle size was 15-35 μm . Initially, 0.5 g of the nanoporous silica gel were immersed in 7 g of 15 wt.% aqueous solution of sodium chloride, and sealed in a polymethyl methacrylate (PMMA) container. The nanopores of the silica gel were of a three-dimensional structure, which have been discussed by Polarz and Smarsly. The sodium chloride was added to improve the gas solubility, so that the phenomena predicted in the MD simulation could be more pronounced. The addition of sodium chloride might increase the complexity of liquid behaviors in nanopores, the details of which are still under investigation. Nevertheless, the major characteristics of infiltration and defiltration were not affected.

By using a type 5569 Instron machine, immediately prior to the infiltration-defiltration experiment, a pre-loading cycle was applied so as to deactivate the inaccessible pores, with the crosshead speed of 0.5 mm/min and the maximum pressure of 40 MPa. The air bubbles in between the silica particles were removed by using a Branson 200 ultrasonic machine before the test. Note that a significant amount of gas molecules were entrapped in the nanopores. As the piston was compressed into the container, the piston displacement, d , and the force acting on the piston, F , could be continuously measured. Denote $A = 286 \text{ mm}^2$ as the cross-sectional area of the piston. The applied pressure was calculated as $P = F/A$, and the specific system volume change was defined as $\Delta V = d \cdot A/m$, with m being the mass of the nanoporous silica gel. When the pressure was low, water could not enter the hydrophobic nanopores, resulting in a relatively linear $P - \Delta V$ relationship with the slope close to the bulk modulus of water. When the pressure was higher than the critical value of 17 MPa, water could be forced into the nanopores as the energy barrier associated with the capillary effect was overcome, leading to the prominent infiltration plateau of the sorption isotherm curve, as shown in Fig. G-4a. The infiltration process was completed when the pressure was 27 MPa. As the applied load was reduced, after the initial linear unloading, the confined liquid came out of the nanopores, forming the defiltration plateau. When the applied pressure was reduced to zero, most of the nanopore volume had been recovered and, therefore, as the loading-unloading cycle was repeated the sorption isotherm curve was nearly the same as the first loop. During the infiltration and defiltration process, the liquid phase was clear and no air bubble could be detected, indicating that the gas phase in the nanopores remained being confined.

The excess gas molecules in the nanopores could be removed through room-temperature diffusion. After the pressure-induced infiltration, if the peak pressure was maintained at 50 MPa for 12 hours, the confined liquid would remain in the nanopores. Initially, due to the dissolution of the entrapped gas, the gas concentration inside the nanoporous silica gel was higher than outside, while over time an equilibrium condition would be reached under the hydrostatic pressure. As a result, the gas molecules diffused out and a large number of air bubbles of the average size of about 0.1 mm appeared. Under this condition, as the applied pressure was subsequently reduced to zero, little defiltration could be observed and therefore the defiltration plateau was quite unclear, as shown in Fig. G-4b. That is, most water remained in the nanopores, which could also be verified from the second loading cycle where very few water molecules could enter the nanopores, i.e. the infiltration plateau was much narrower compared with that of the first loading. Under the atmosphere pressure, the total volume of the air bubbles appeared after the high-pressure resting, normalized by the mass of silica gel, was about $0.35 \text{ cm}^3/\text{g}$, smaller than but close to the accessible nanopore volume. Clearly, during the holding at peak pressure, the reduction in gas concentration in nanopores significantly enhanced the confinement effect of pore walls and resulted in the “non-outflow” of the confined liquid. In other words, the gas phase inside the nanopores provided a critical driving force of defiltration, absence of which would cause difficulties of liquid motion, as predicted by the MD simulation. The ARO supported the theoretical analysis of this study, as well as the matching experimental investigation.

H. Calometric Measurement of Liquid Infiltration in Nanopores

In order to understand the energy exchange process, we investigated a nanoporous silica gel. The material was obtained from Sigma-Aldrich. By using a Tristar-3000 Gas Absorption Analyzer, its average nanopore size was determined to be 16.1 nm; its specific surface area was 305 m²/g; and its specific nanopore volume was 1.07 cm³/g. The particle size was 200-500 μm. The as-received material was hydrophilic, and thus when it was immersed in water it would be soaked up spontaneously. To produce an energy absorption system, it must be surface treated. After the silica gel had been dried in vacuum at 100 °C for 24 h, it was treated at 90 °C for 24 h in a round-bottom flask in 40 ml of dry toluene and 1 ml of chlorotrimethylsilane, with the mixture being stirred at the rate of about 30 rpm. Then, the silica gel was collected by vacuum filtering, washed by dry toluene and warm water repeatedly, and vacuum dried. During the surface treatment, the hydroxyl groups at nanopore surfaces were deactivated.

Figure H-1 depicts the setup of infiltration experiment, which consisted of a double-layer cylinder. The outer layer was made of stainless steel, and the inner layer was made of Teflon. The thickness of the inner layer was 12.6 mm. The cylinder contained 1.0 g of surface treated silica gel and 5 g of deionized water. According to a differential scanning calorimetry measurement, the specific heat of the mixture of silica gel and water was 3.4 J/g·K. A quasi-hydrostatic pressure was applied on the liquid phase through a stainless steel piston. The piston was insulated from the liquid phase by a 12.6 mm thick Teflon layer. The average temperature in the central part of the cylinder was measured by three type E thermocouples, with the accuracy of 0.05 °C. By using warm water to calibrate the system, it was confirmed that the insulation property was quite good. The temperature decrease was smaller than 0.1 °C within 20 sec.

By using a type 5569 Instron machine, the piston was intruded into the cylinder at a constant rate of 7.5 mm/min. As the inner pressure reached 10 MPa, it was moved out at the same rate. The loading-uploading cycle took 10-15 sec. The set point of 10 MPa was chosen so that the nanopores would not be fully filled, as will be discussed shortly. Figure H-2 shows typical sorption isotherm curves. If the loading rate was changed to 1 mm/min, no detectable variation in sorption curves could be observed, indicating that such a loading rate could be regarded as quasi-static. During the infiltration experiment, the temperature inside the cylinder was measured continuously. For comparison purpose, a similar testing procedure was repeated on a reference system which contained only 5 g of deionized water but no silica gel. Table 1 shows the measurement results.

It is remarkable that, according to Table H-1, no significant temperature increase can be detected during the liquid water infiltration. As shown in Fig.H-2, initially, when the pressure is relatively low, liquid water cannot enter the nanopores. Thus, the pressure increases from “A” to “B” quite linearly. The slope of the sorption curve is dominated by the liquid compressibility and the machine compliance. The specific volume change is defined as the volume occupied by the piston per unit mass of silica gel. It is clear that after the surface treatment it is energetically unfavorable for the liquid to wet the nanopore surfaces. When the pressure is about 8.7 MPa, the liquid phase starts to enter the nanopores. The pressure induced infiltration continues to “C”. In the infiltration plateau (“BC”), the system compressibility is much larger than that in Section “AB”. When the peak pressure of 10 MPa is reached, the piston is moved out of the cylinder, so that the inner pressure decreases. The unloading path, “CD”, is different from the loading path, “ABC”, which suggests that the confined liquid does not defiltrate. The slope in Section “CD” is similar to that of “AB”, both of which are dominated by the compressibility of liquid water as well as the machine compliance. The infiltration volume is nearly 0.3 cm³/g, only one third of the specific nanopore volume. Note that in the infiltration process, the system volume change is quite independent of the liquid compressibility. If the peak pressure were increased, more nanopores would be involved in the pressure induced infiltration and the complicated gas dissolution may affect the testing results.

When unloading is completed, at the second loading, the system compressibility is lost. Since the nanopores are filled, no more liquid infiltration can be observed, and both loading and unloading paths are linear. That is, upon the first unloading, the compressed gas phase cannot repel the confined liquid as the pressure is lowered. There are a few possible reasons of the non-outflow phenomenon, including the nonuniform nanopore structure, e.g. the “ink-bottle” effect,²¹ the hysteresis of effective contact angle,²² etc., the details of which are still under investigation.

During the first loading, mechanical work is stored as compression strain energy in the liquid phase before infiltration starts, which can be assessed as the area under Section “AB”, W_e . As the liquid infiltrates into the nanopores, the external pressure must be maintained at a high level, and associated with the system volume decrease the mechanical work done by the piston can be estimated as the area under Section “BC”, W_{in} . During unloading, since the slopes of “CD” and “AB” are close to each other, W_e is released, while W_{in} is effectively dissipated. In the current system, W_{in} is about 2.9 J. If W_{in} were converted to thermal energy, since the heat capacity of the silica-water mixture is 3.4 J/g·K, the system temperature should increase by 0.84 °C, which is not detected in the experiment. Table 1 shows that, compared with the reference system where no silica gel is added, the temperature change of the NMF liquid is nearly the same.

Figure H-3 depicts the liquid motion in a nanopore. If liquid molecules slide against the solid surface, since they must overcome periodic energy barrier to move among tetrahedral sites, when they reach a metastable state excess energy can be transferred to the environment. Thus, the system temperature should rise. Because the temperature change is negligible, the conventional no-slip boundary condition may still be valid. One way to explain this result is to take into consideration the conversion of mechanical work to solid-liquid interfacial tension. As the nanopore surface is exposed to the liquid phase, the interfacial tension, γ_{sl} , is larger than $\gamma_s + \gamma_l$, with γ_s and γ_l being the surface tensions of the solid and the liquid, respectively. If the excess interfacial tension, $\Delta\gamma = \gamma_{sl} - (\gamma_s + \gamma_l)$, equals to W_{in}/A , no work can be converted to thermal energy, where A is the total pore surface area. In the current system, the mass of silica gel is 1 g, with the total surface area of 305 m². Thus, $\Delta\gamma = 9.5 \text{ mJ/m}^2$. Since the solid structure is much more rigid than the structure of liquid molecules, the majority of the excess interfacial tension should be stored in the liquid phase, causing a variation in average molecular distance. For a first order approximation, the inner pressure inside the nanopores can be taken as the infiltration pressure, which is around 9.5 MPa. Thus, across a unit area of nanopore surface, the volume variation that causes $\Delta\gamma$ is $2 \times 10^{-9} \text{ m}^3$, about 50% of the corresponding nanopore volume. That is, the average distance among the confined liquid molecules varies by nearly 20%, which looks plausible. Because most of the mechanical work is consumed to overcome the capillary effect and stored as the interfacial energy, little thermal energy can be generated, so that the temperature variation is within the resolution of the testing system.

In another experiment, we investigated a nanoporous silica of a smaller nanopore size. The testing device is depicted in Fig.H-4(a). It consisted of a stainless steel outer shell and a Teflon inner shell. A steel piston, which was sealed by a reinforced gasket and insulated by a Teflon layer, could be compressed into the cylinder by an external pressure, P . The cylinder contained nanoporous silica gel particles suspended in 4 g of saturated aqueous solution of sodium chloride. The mass of nanoporous silica gel was in the range of 0.1 to 1.0 g. It was obtained from the Sigma-Aldrich, with the average nanopore size of 8 nm and the specific nanopore volume of 0.5 cm³/g. The as-received material had the particle size of about 50 μm . It was first degassed in vacuum at 100 °C for 12 h, and then refluxed in 2.5% dry toluene solution of chlorotrimethylsilane (CTMS) at 90 °C for 48 h. Since CTMS molecules were much smaller than the nanopore size, they could react with the hydroxyl sites at nanopore surfaces, forming a monolayer of silane groups. Finally, the material was washed by toluene and dried in a vacuum furnace at 100 °C for 12 h. A part of the silica gel suspension was sealed in a polyisoprene (PI) cell, which was immersed in the rest of the suspension in the testing cylinder. The PI cell as well as the liquid phase outside it acted as additional insulation media. Inside the PI cell, the temperature was

recorded by a type E thermocouple. The heat capacities of the silica gel suspensions were 4.0 J/g·K, 3.9 J/g·K, 3.8 J/g·K, 3.7 J/g·K, and 3.5 J/g·K, as the silica gel masses were 0.1 g, 0.25 g, 0.5 g, 0.75 g, and 1.0 g, respectively.

In a type 5580 Instron machine, the piston was driven downward at a constant rate. The loading rate ranged from 0.5 mm/min to 30 mm/min. The cross-sectional area of the piston, A_0 , was 286 mm². The quasi-static pressure in the liquid phase, P , was calculated as the piston force divided by A_0 . The volume change of the silica gel suspension was calculated as the piston displacement multiplied by A_0 . Unloading was performed at the same rate after P exceeded 50 MPa. Figure 2 shows typical pressure-time and temperature-time curves. For each set of loading rate and silica gel mass, 3-4 samples were tested, and the results of temperature variations are shown in Figs.3 and 4. For each sample that contained 0.75 g of silica gel, at the loading rate of 2 mm/min., the infiltration-defiltration loops were repeated for 10 times.

Since the silane group coated nanopore surface is nonwetable, the nanopores would remain empty as the nanoporous silica gel is immersed in water. With the addition of sodium chloride, the effective degree of hydrophobicity is further increased, and the difficulty in defiltration is much reduced. As depicted in Fig.H-4(b), if the external pressure applied by the piston is relatively low, the silica gel suspension is quite rigid, with the compressibility being dominated by the free liquid phase. When P reached the critical value to overcome the capillary effect, infiltration is induced and an infiltration plateau is formed in sorption curve (“AB”). After the nanopores are filled, the slope of Section “BC” is similar with that of “OA”. During unloading, defiltration happens at a pressure level much lower than that at “A”, leading to a linear return section, “CD”. From “D” to “O”, as the confined liquid comes out, there is a defiltration plateau. After the first loading-unloading cycle, the sorption curves are nearly identical in all the following cycles. Due to the large deformability of the insulation layers and PI cells, in the current study the onset and ending sections of infiltration and defiltration plateaus are relatively unclear, compared with previous results of solid steel testing cells. Nevertheless, effective transition points can be defined at the locations where the slopes of sorption curve equal to the average values of the slopes in Sections “OA” and “AB”.

In such a hysteretic sorption-desorption process, the absorbed mechanical work equals to the area enclosed by the loading-unloading cycle, which is nearly 11 J per gram of silica gel [22]. If it is dissipated as heat, for the system containing 0.75 g of silica gel, it would result in a temperature increase $\Delta T_0 = 0.48$ °C. Figure H-5 shows that, during infiltration, in Section “AB”, the temperature indeed largely increase. However, the temperature change, ΔT_{in} , is nearly 1 °C, almost two times higher than the predicted value. Before the infiltration starts, in Section “OA”, the temperature variation is negligible, confirming that the elastic compression of free liquid phase and empty nanoporous silica gel particles is isothermal. After the infiltration completes, but before the defiltration begins, from “B” to “D”, the temperature variation is also quite small; that is, loading and unloading on filled nanoporous silica gel suspension would not cause heat generation or loss. As the confined liquid comes out of the nanopores, during the defiltration plateau (“DE”), temperature decreases, after which, at rest, the system temperature does not vary. The temperature decrease in “DE”, ΔT_{de} , is smaller than the temperature increase in “AB”. Consequently, after the loading-unloading cycle, there is a net residual temperature variation of 0.45 °C, close to the value of ΔT_0 estimated from the dissipated mechanical work.

Clearly, there are two parts of the temperature increase in infiltration: one is reversible and the other is irreversible. The reversible part is recovered during defiltration, and the irreversible part leads to the residual temperature variation; that is, $\Delta T_{in} \approx \Delta T_{de} + \Delta T_0$. Both ΔT_{in} and ΔT_0 are quite linear to the mass of silica gel, m . As shown in Fig.H-6, when m is only 0.1 g, ΔT_0 is about 0.1 °C and ΔT_{in} is around 0.2 °C. When $m = 0.5$ g, they are 0.3 °C and 0.9 °C, respectively. When $m = 1$ g, they become 0.6 °C and 1.5 °C, respectively. According to the energy dissipation calculated from the sorption curves, the residual temperature changes should respectively be 0.07 °C, 0.17 °C, 0.33 °C, 0.48 °C, and 0.64 °C, for systems of silica masses of 0.1 g, 0.25 g, 0.5 g, 0.75 g,

and 1.0 g, which are close to the measured ΔT_0 . The slight nonlinearity may be caused by the change in specific heat. In all the systems, the residual temperature changes are 30%-60% of the maximum temperature increases, suggesting that the magnitudes of the two parts are comparable with each other. The correlation between temperature variation and silica mass indicates that the exothermic and endothermic processes are related to liquid infiltration and defiltration in nanopores.

Note that, although the temperature change in a single loading cycle is relatively small, for damping systems that work under cyclic loadings the heat generation must be taken into consideration. Because the confined liquid can defiltrate after the external pressure is reduced, after a full cycle of loading and unloading, the system would return to its initial configuration. If similar cycles are applied, it can work continuously. During each loading cycle, the characteristics of temperature change are identical. As a result, the temperature keeps increasing by ΔT_0 in each loop. After only a few cycles, the overall temperature changes by 3-4 °C. That is, the nanoporous silica gel suspension acts as a heat source, converting mechanical work to thermal energy.

Figure H-7 shows that, both ΔT_{in} and ΔT_0 are insensitive to the loading rate. As the loading rate increases from 0.5 mm/min to 30 mm/min, the variations of maximum and residual temperature variations are less than 10%. In the range of 2 mm/min to 30 mm/min, little statistically meaningful changes can be observed, which suggests that the liquid motion in nanopores is quite non-viscous, as observed in computer simulations and experiments on nanotubes and nanopores. The weak loading rate dependence of temperature change may not be intrinsic. As the loading rate is smaller, it takes longer time to complete an infiltration-defiltration loop, and thus the loss of generated heat increases. Moreover, at a higher loading rate, the compression of silica gel suspension can be less regular, causing shear flow among different sections of the liquid phase. Due to the friction of silica gel particles, a certain amount of energy can be dissipated, somewhat similar with the loading rate effect in a shear thickening liquid.

The reversible part of temperature variation may be related to the resistance to the motion of liquid molecules. As a liquid molecule moves along a large solid surface, its distance to the solid atoms tends to vary [29]. At a tetrahedral site, the liquid-solid distance is smaller, since the resultant forces from the solid phase reaches the minimum value. In between tetrahedral sites, the liquid molecule moves toward the interior, so that the energy barrier is reduced. In a nanopore, however, the motion of liquid molecules normal to the solid surface is considerably constrained. Thus, the effect of the energy barrier becomes more pronounced. In order to overcome the energy barrier, the system free energy must increased by the external pressure. As the energy barrier is bypassed, the excess kinetic energy of the liquid molecule may be absorbed by the adjacent solid atoms, so as to keep the effective infiltration rate constant. During this process, heat is generated and the system temperature increases. During defiltration, the confined liquid molecules bypass the energy barrier with the aid of thermal vibration, and thus they absorb heat from the environment, causing a temperature decrease. Since the energy barrier is independent of the direction of liquid molecule motion, the associated temperature increase and decrease should be the same.

The irreversible part of temperature variation may be associated with the nonlinear relationship between the mobility of confined liquid molecules and the applied pressure, which makes the infiltration and defiltration process hysteretic. It may also be attributed to the imperfect nanopore structure. For instance, if the nanopore diameter varies in a certain range, across a “bottleneck” site the liquid motion can be quite different with or without an external pressure, resulting in additional hysteresis. Furthermore, the silane groups that cover the nanopore surface may not be uniform. Their density may be higher close to the open end of a nanopore and lower in the interior. Thus, since infiltration starts from the outside and defiltration starts from inside, the loading and unloading paths tend to be different. The role of entrapped gas molecules in nanopores can also be fundamentally different from that in larger pores, which may either block or promote infiltration and defiltration, depending on the nanoporous structure, the host and guest species, as well as the working pressure.

I. Upper Limit of Energy Absorption Efficiency

One question that remains unanswered is: what is the upper limit of the energy density of NMF liquids. As discussed above, the energy density increases with $\Delta\gamma$. In order to enhance the energy absorption performance, so that minimum amount of nanoporous material is needed to dissipate a specified amount of energy, materials of large surface areas and solid-liquid systems of high interfacial tensions must be used. If the liquid phase is water based, usually $\Delta\gamma$ is around 10 mJ/m². While a number of techniques, such as surface modification of nanoporous materials and adjustment of liquid composition have been developed, the improvement is usually 20%-50%. To achieve a higher interfacial tension, liquids of much larger surface energies, such as liquid metals, should be employed. In this article, we focus on the mechanical behaviors of NMF liquids. We attempt to estimate their maximum possible energy density, which provides a basis for materials selection and structural optimization. To determine the upper limit of this technique, we investigated a nanoporous material of a large surface area, commonly known as mobil crystalline material (MCM) 41. By using a liquid metal, both interfacial tension and nanopore surface area are close to the maximum possible values, so that the energy density represents the upper limit that can be reached by using a NMF liquid. The network material was obtained from The Sigma-Aldrich (CAT No. 643745). In order to increase the free energy of nanopore surface, the material was treated in a 2.5% dry toluene solution of chlorotrimethylsilane, following a vacuum drying at 100 °C for 24 h. The treatment temperature was maintained at 20 °C for 10 min, with the mixture being stirring continuously, and then at 90 °C for 1 h, as the solution is refluxed. Then, the MCM41 was collected by vacuum filtering, washed in dry toluene and warm water, and vacuum dried repeatedly. During the surface treatment, silane groups were formed at hydroxyl sites, modifying the nanopore surface structure. The surface treated MCM41 was analyzed in a Tristar-3000 Gas Absorption Analyzer, and its nanopore surface area distribution is given in Fig.I-1. The modal value and the average value of pore size were 2.4 nm and 3.5 nm, respectively. The specific surface area was 807 m²/g; and the specific pore volume was 0.8 cm³/g.

The liquid metal was chosen as mercury (Hg). About 0.2 g of MCM41 was sealed in a stainless steel cylinder, together with 5 cm³ of mercury, as depicted in Fig.I-2. Since the nanopore surface was nonwettable to Hg, at rest the nanopores would remain empty. By applying a quasi-static pressure through a piston, Hg atoms could be forced into the nanopores, and thus the system volume decreased considerably, as shown in Fig.I-3. As the pressure reached the set point, the piston was moved out of the cylinder. Once the pressure was reduced to zero, the same loading procedure was repeated, and the system behavior at the second loading was observed. The maximum pressure varied from 160 MPa to 300 MPa. As the maximum pressure increased, smaller nanopores could be involved in the pressure-induced infiltration (PII), and thus the infiltration volume became larger. It was noticed that as the pressure exceeded 200 MPa, the infiltration volume was constant 0.8 cm³/g, indicating that nearly all the nanopore surface was exposed to the Hg phase. Under this condition, the system properties are summarized in Table I-1.

Even at a relatively low pressure, the sorption isotherm curves shown in Fig.I-3 are of finite slopes, which are primarily determined by the mechanical compliance of the experimental setup and the bulk modulus of mercury. When the pressure reached about 100 MPa (point “A” in Fig.3), the slope abruptly reduces, indicating that the system compressibility becomes much larger. Clearly, as the capillary effect of nanopores is overcome, the liquid phase enters the empty space inside the MCM41 particles, and consequently the system volume decreases. The liquid infiltration does not take place in all the nanopores simultaneously. According to the classic Laplace-Young equation, the required infiltration pressure is $P_{in} = 4\cdot\Delta\gamma/d$, where d is the pore size. Thus, infiltration starts in the largest nanopores. Once these pores are filled, the pressure must be increased to a higher level to induce infiltration in smaller nanopores, which is indicated by the change in the slope of infiltration (“AB”) of sorption isotherm curve. According to Fig.I-1, the largest nanopore size is around 4 to 5

nm. Since at the onset of pressure induced infiltration (point “A” in Fig.3), the pressure $P_{in} = 102$ MPa and $\Delta\gamma \approx 128$ mJ/m², which is much higher than that of aqueous solution based systems.

As the peak pressure is reached and the piston is moved out of the cylinder, the unloading path is quite different from the loading path, causing a pronounced hysteresis. The slope of unloading path is similar to the slope in section “OA”, which suggests that the confined mercury molecules do not defiltrate, even when the peak pressure is relatively low and the nanoporous space is only partly filled. That is, the compressed gas phase in a MCM41 particle cannot overcome the “self-locking” effect, which may be attributed to the “ink-bottle” effect associated with the irregular nanopore structure, the breakdown of gas nanobubbles, and/or the formation of new bonds between liquid molecules and nanopore walls. Since the interfacial tension cannot be released upon unloading, the mechanical work done by the loading path is effectively dissipated. As shown in Table 1, in the first loading cycle, the absorbed energy density is $E = 140$ J/g. It is the highest value that has been achieved by using NMF liquids. Since in the MCM41-Hg system both interfacial tension and surface area are close to the maximum possible values of nanoporous processing technology, this value indicates the upper limit of system performance.

As the energy absorption capacity is fully utilized (i.e. when the maximum pressure is higher than 200 MPa), the specific infiltration volume, which is defined as the system volume decrease normalized by the mass of MCM41, is about 0.8 cm³/g, nearly the same as the porosity measured in the gas absorption analysis. Therefore, the energy absorption should be achieved across the entire nanopore surface. The value of $\Delta\gamma$ can be assessed as $\Delta\gamma = E/A = 173$ mJ/m², comparable with but larger by 26% than the estimation based on the Laplace-Young equation, probably because of the sub-nm features at nanopore surfaces that make the assumption of circular nanopore cross section less relevant.

After the first loading-unloading cycle, since the nanopores are filled by mercury, as the external pressure is applied again, little infiltration can be observed. That is, energy absorption can be achieved only at the first loading, and such a system is suitable for one-time protection applications, such as for car bumpers. Before the PII experiment, the MCM41 particles are white powders, with the average particle size of 50 μ m and the density of 0.4 g/cm³. The weight density is about 5 times smaller than that of bulk silica (2.1 g/cm³), in agreement with the fact that the porosity is nearly 80%. After the PII experiment, the MCM41 particles form large aggregates, with the size around 1-2 mm. The weight density largely increases to 11 g/cm³. Clearly, the nanopores are filled by mercury. The effective density of the confined mercury is around 13 g/cm³, nearly the same as the specific weight of bulk mercury, suggesting that the atomic structure of mercury phase in nanopores may be similar to that in bulk phase.

Note that the MCM41-mercury system may not be directly useful to industrial fields due to cost and environmental concerns. Nevertheless, the current study gives the upper limit of the performance of NMF liquids. As long as the required energy absorption effectiveness is lower than 140 J/g, this technique is relevant; otherwise new protection mechanisms must be discovered. It is envisioned that if other liquid metals, such as tin and gallium, are used, the system can be much more environmental friendly.

J. Compression of Nanoporous Particles

One intrinsic difficulty in developing higher-performance cellular materials is related to the relatively long characteristic time of cell-wall buckling. As an order-of-magnitude approximation, the buckling time, t_b , may be taken as $1/\omega$, where ω is the resonance frequency of cell wall. For a cantilever-beam-type structure, $t_b = \alpha^* \sqrt{\rho/EI} \cdot d^2$, where d is the cell size, ρ is the weight density, EI is the bending stiffness, and α^* is a geometry factor around 0.1-0.3. For most of engineering cellular materials, t_b is in the range of a few milliseconds to a fraction of second, longer than the travelling time of a stress wave across the cell. Therefore,

while cell-wall buckling can significantly lower the peak pressure, the profile of wave front is often not affected. In order to solve this problem, t_b must be decreased to the μs or sub- μs level, for which the cell size, d , needs to be reduced by a few orders of magnitude to the nm scale. This concept can also be regarded as the promotion of high-order buckling modes. If the cell wall size is large, the first-order mode is most energetically favorable.¹² Recent research has shown that if soft joints are installed, they would trigger higher-order buckling modes under a relatively low pressure, and thus both temporal and spatial characteristics of buckling patterns are adjusted.¹³ Decreasing the cell size can be of a similar effect. As a large cell breaks down into a number of smaller ones, the motion of cell walls parallel to the external loading would be constrained by the cell walls normal to the loading, and thus low-order buckling modes cannot take place.

Nanoporous materials functionalized (NMF) liquids can be utilized to fill the cells in a regular cellular material so as to enhance its performance. In such a system, it was observed that in addition to the infiltration of pressurized liquid, the eventual collapse of nanoporous structure also provided a beneficial energy-absorption mechanism. In order to investigate nanoporous silica behaviors, a silica hydrosol was first produced by refluxing water glass that contained 5.6% Na_2O and 14.9% SiO_2 and 3M sulphuric acid solution. Silica hydrosol was extracted by a needle valve. The reactor was kept in a water bath at room temperature. The pH value was maintained at 3.5, so that the specific micropore volume was minimized. The hydrosol was washed in distilled water repeatedly, and set for 24 h, leading to the formation of nanoporous silica gel. The gel particles were then dried in a continuous air flow at 100 °C for 3 h. Their nanoporous structure was characterized by using a Micromeritics TriStar-3000 gas absorption analyzer, and the results of nanopore volume and nanopore surface area distributions are shown in Fig.J-1(a) and (b), respectively.

The synthesized nanoporous silica gel particles was placed in an air-hardened steel cylinder and compressed by a steel piston. By using a type 5569 Instron machine, the piston was moved into the cylinder at a constant rate of 1 mm/min. At the first loading, when the pressure reached 200 MPa, the piston was moved out at the same rate. The same loading-unloading process was repeated, after which the loosely packed particles were consolidated into a disk. Then, with the same loading rate, the nanoporous silica disk was compressed to 750 MPa for two cycles. Figures J-2 and J-3 show typical load-displacement curves. After each loading, about 0.1 g of silica gel was harvested for gas-absorption analysis, following which the samples were dissolved in methanol and dried by vacuum filtering, and then their weight densities were measured. The data of nanoporous structures are listed in Table J-1. The dried sample was also observed in an environmental electron scanning microscope (SEM). Figure J-4 shows typical micrographs.

The results of the porosity analysis in Fig.J-1 indicate clearly that the synthesized silica gel is mesoporous. The nanopore volume distribution curve has the modal value of 9.4 nm. The most probable nanopore size in the surface area distribution curve is slight smaller, around 8.3 nm, since larger nanopores have smaller specific surface areas. Most of the pore volume is associated with the nanopores of sizes in the range of 5-15 nm; the contribution of nanopores smaller than 3 nm or larger than 18 nm is negligible. However, the surface area of the smallest nanopores is only slightly smaller than the peak value.

In the low-pressure compression test, as shown in Fig.J-2, no clear pressure plateau can be observed. With the increasing of compression volume, the pressure increases gradually to the set point of 200 MPa. As the load is reduced, while initially the unloading path and the loading path overlap with each other, the linearity of the unloading curve is maintained quite well even in the low-pressure range, until the external load entirely vanishes. Thus, there is a significant residual deformation, primarily due to the close-packing of the silica particles. The changes in nanopore surface area distribution and nanopore volume distribution are quite small (Fig.J-1), suggesting that the nanopores remain stable. This is confirmed by the SEM observation that before (Fig.J-4a) and after (Fig.J-4b) the low-pressure compression experiment the frameworks of silica particles are similar. The relative probability of nanopore size distribution at the peak value decreases by about 8%, and that of the smallest nanopores slightly increases, i.e. a small portion of large nanopores are broken down into smaller

ones, probably related to the collapse and fracture of the nanopores close to particle surfaces. The change in porous structure in the largest nanopore size range is not detectable. There are no considerable variations in the average nanopore size, the total nanopore surface area, the total nanopore volume, as well as the weight density.

As the second loading cycle is applied, the compressibility of the particle cluster becomes much smaller. Compared with the first loading path, the pressure reaches the peak value with a much smaller displacement. The slope of the compression curve is close to that of the final linear stage of the first loading. The unloading path is nearly identical with the loading path, and both of them are about the same as the first unloading path; that is, the packing of silica particles has been saturated.

When the nanoporous silica disk is compressed at a higher pressure, as shown in Fig.J-3, the testing curve exhibits entirely different characteristics. As the pressure is relatively low, the loading path resembles that of the low-pressure test. When the pressure exceeds about 400 MPa, the slope considerably decreases, indicating that the system compressibility increases. In the pressure range of 400-650 MPa, a plateau is formed. The width of the plateau is about $0.5 \text{ cm}^3/\text{g}$, quite close to the specific nanopore volume. SEM microscopy (Fig.J-4c) indicates that the silica particles are crushed and fractured. When the pressure is higher than this range, the system compressibility rapidly decreases. Upon unloading, the pressure-displacement curve is relatively linear, except for the final low-pressure section. The slope of the high-pressure section of unloading path is similar with the slope of the final stage of loading path. The high degree of hysteresis causes a large residual deformation. As the high-pressure loading-unloading cycle is repeated, the system behavior becomes quite linear. No compression plateau can be observed. Both the loading and the unloading paths are of similar slopes with that of the unloading path of the first cycle.

According to the TriStar-3000 analysis, after the high-pressure compression, the nanopore volume distribution changes considerably. Clearly, the compression plateau in Fig.J-3 is associated with the collapse of nanopores. The maximum volume decreases by nearly 50%, and the peak becomes flatter, i.e. the nanopore volume distributes over a broader range of nanopore size. The volume of relatively small nanopores increases, which suggests that larger nanopores are “shrunk” or broken down into smaller nanopores. The changes in nanopore surface area distribution are of similar characteristics. The percentage of nanopores larger than 5 nm largely decreases, while in the nanopore size range of 2-5 nm a relatively high plateau is observed. The peak value is only slightly lower than that of uncompressed sample, while the location of the peak shifts toward the lower end by about 3 nm. Note that the overall specific nanopore surface area changes by only 2%; that is, existing nanopore surface does not vanish.

During the high-pressure loading, the nanopore structure is compressed by $0.5 \text{ cm}^3/\text{g}$. At the peak pressure, the nanopore space should be nearly entirely compressed. After unloading, the gas absorption analysis shows that there is a large residual nanopore volume of $0.34 \text{ cm}^3/\text{g}$, i.e. the nanoporous structure is partly recovered as the external load is fully removed, which fits with the observation that the slope of unloading curve rapidly decreases in the low-pressure stage. The recovered nanopores do not carry load at the second loading, and thus they must be formed by damaged walls. The weight density of the initial material is $742 \text{ mg}/\text{cm}^3$. Since it contains $0.54 \text{ cm}^3/\text{g}$ of nanoporous space, the effective density of the network material is $1.6 \text{ g}/\text{cm}^3$. The weight density of the high-pressure compressed material is $1128 \text{ mg}/\text{cm}^3$, and therefore the effective density of network is $1.7 \text{ g}/\text{cm}^3$, close to the initial value, as it should be.

The collapse of nanopores provides a mechanism for plastic deformation. Usually, in a ceramic material elastic deformation is dominated by atomic bonding and plastic deformation is governed by behaviors of dislocations or atomic clusters, both of which are of characteristic lengths around 1 to 10 nm. Since ordinary plastic-deformation mechanisms are inactive at room temperature, when being compressed the pressure and the strain in a solid silica would increase linearly, and once the critical pressure is reached cleavage fracture would occur. With the large volume fraction of nanopores, the silica gel behaves as a ductile material. Even though the network is brittle, due to the change of nanoporous structure, which is of a length scale comparable with that of

a dislocation or an atomic cluster, the overall deformability is largely improved. Figure J-5 depicts two possible collapse modes of a nanopore. In mode “a”, the nanopore walls parallel to the external loading buckle. According to the classic linear elastic beam theory, the buckling stress can be assessed as $\sigma_1 = \alpha E \rho / \rho_0$, where $\alpha \approx 0.05$ is a system parameter, E is the modulus of elasticity, ρ is the weight density of nanoporous phase, and ρ_0 is the weight density of network. For the silica gel investigated in the current study, as discussed above, $\rho = 0.74 \text{ g/cm}^3$ and $\rho_0 = 1.6 \text{ g/cm}^3$. If E is taken as 20 GPa, the value of σ_1 is about 500 MPa, close to the measurement result. In mode “b”, the reduction in nanoporous structure is caused by the bending and associated failure of nanopore walls normal to the external loading, for which the critical stress can be estimated as $\sigma_2 = \bar{\alpha} Y (\rho / \rho_0)^{3/2}$, where $\bar{\alpha} \approx 0.3$ is a system parameter and Y is the strength of network material, which is 1-2 GPa for silica. Thus, σ_2 is around 100-200 MPa, much smaller than the measured pressure of compression plateau. It can be seen that the change in nanoporous structure should be dominated by mode “a”. Although mode “b” requires a lower stress, it is suppressed, probably due to the irregular configuration and the contoured paths of nanopores, the interconnected nanopore structure, etc.

The energy absorption capacity related to the nanopore collapse can be calculated as the area enclosed by the loading-unloading cycle, which is nearly 300 J/g. This value is higher by orders of magnitude than that of many conventional protection and damping materials, such as reinforced polymers and shape memory alloys. It is also much higher than that of NMF liquids. For instance, if the nanoporous silica gel is surface treated and immersed in an aqueous solution of electrolyte, the energy absorption efficiency is 10-30 J/g. Even if liquids of larger surface tensions are utilized, the maximum energy absorption efficiency is only about 100 J/g. The high energy absorption performance of the nanoporous silica gel should be attributed to the small nanopore size, the relatively large porosity, as well as the high network strength.

K. Ion-Solid Interaction in Nanopores

At the inner surface of a nanotube or a nanopore where the tube/pore size is comparable with the Debye distance, the classic interface theory is no longer valid. As the volume to surface area ratio becomes small, the bulk liquid phase does not exist. Since the cation-solid and anion-solid interactions are different, the confined liquid can be of a net electric charge, especially when the system is subjected to an external mechanical, electric, or thermal loading. The nanotube/nanopore wall also strongly constrains the solvated structure and the ion diffusion. If the space is insufficient, the ions may not be fully solvated. The anions may contact the solid surface, resulting in a “squeezing” effect. Under controlled conditions, the unique liquid structures in nanotubes or nanopores tend to cause higher molecular/ionic transport rates. If the environment varies, it may take a long time for the confined liquid to reach the new equilibrium condition, since the bulk “reservoir” phase is absent and the molecules and ions must diffuse along the axial direction. At the nanometer scale, the repelling effect of solid surfaces can be pronounced. Even if the nanopore surface is wettable and a large driving force is applied, the nanopore size must be much larger than the solvent and solute molecules.

Although investigations have been intensively carried out in this area, the research is still at its early stage, partly because of the difficulties in direct observation of ionic behaviors in nanotubes/nanopores and the lack of systematic testing data. In the current research, to investigate the effect of ion size in nanoenvironment a MCM-41 was synthesized. In a polypropylene bottle, 4 parts of SiO_2 , which was provided as a water glass that contained 14% sodium hydroxide and 27% silica, 1 part of cetyltrimethyl ammonium bromide (CTAB), 1.1 parts of sodium oxide, 0.3 parts of ammonium hydroxide, and 200 parts of deionized water were stirred vigorously for 1 h at room temperature. By dropping acetic acid into the mixture, the pH value was kept at 10. After addition of 15% sodium chloride solution, the liquid became single-phased and clear. It was sealed in an autoclave at 95 °C for 72 h. The particles were collected by vacuum filtering and washed by warm water, and

dried at elevated temperature. The nanopores were created by combusting the material at 550 °C for 6 h, so that the template was removed. In order to reduce the effective nanopore size and to modify the nanopore surfaces, the MCM-41 particles were vacuum dried at 100 °C for 24 h, and then fully exposed to dry toluene that contained 2.5% chlorotrimethylsilane at 95 °C for 36 h. The byproduct of chlorine acid was removed by repeated rinsing with dry toluene and warm water and vacuum drying at 50 °C.

The nanoporous structure of the surface-treated MCM-41 was characterized by a Micrometrics TriStar-3000 Porosimetry Analyzer through the Barret-Joyner-Halenda (BJH) method. The average nanopore diameter was 2.1 nm, with the standard deviation of 0.2 nm. The specific surface area was 620 m²/g. In a stainless steel cylinder, the MCM-41 particles were sealed with deionized water or 5M aqueous solution of lithium chloride (LiCl), sodium chloride (NaCl), potassium chloride (KCl), or cesium chloride (CsCl). A steel piston was intruded into the cylinder at 0.5 mm/min by a type 5582 Instron machine. The cross-sectional area of the piston, A_p , was 286 mm². When the piston load, F , reached about 25 kN, it was reduced back to zero with the same quasi-static loading rate. Figure K-1 shows typical sorption curves, where the applied pressure is calculated as F/A_p and the system volume change is taken as $A_p \cdot d_p$, with d_p being the displacement of the piston.

With the hydrophobic silyl groups on the inner surfaces of nanopores, the MCM-41 particles cannot be soaked by the liquid phase without the aid of pressure. With the increasing of the applied pressure, P , initially the system volume decreases relatively slowly, as shown in Fig.K-1. For an electrolyte solution based system, when P reaches about 30 MPa, the ratio between the system volume change and the pressure largely increases, indicating that liquid begins to enter the nanoporous space. Because the pore size distributes in a certain range, the slope of the infiltration plateau is always positive, and the profile reflects the nanopore volume distribution. When P increases to more than 40 MPa, the infiltration plateau ends. When unloading is performed, the sorption curve is quite elastic when P is higher than about 22 MPa. In the pressure range of 9 to 22 MPa, there is a defiltration plateau in the sorption curve, where the liquid molecules come out of the nanopores. Eventually, when the nanopores are empty, the unloading curve becomes identical to the lower-pressure section of the loading curve. For self-comparison purpose, in this article the infiltration pressure, P_{in} , and the defiltration pressure, P_d , are respectively defined as the pressures at the middle points of the infiltration and defiltration plateaus. The middle point is set as the intersection of the sorption curve and the middle line between the low-pressure and high-pressure linear sections. When the liquid phase is deionized water, the sorption curve is similar with that of electrolyte solutions, while P_{in} and P_d are much lower, in agreement with the variation in effective surface tension.

It is clear that the infiltration pressure decreases as the cation size increases (Fig.K-2). The ionic radii of cesium, potassium, sodium and lithium are respectively 1.67 Å, 1.38 Å, 1.02 Å, and 0.76 Å. Compared with P_{in} , the variation in defiltration pressure is less pronounced. For the LiCl solution based system, P_d is 15.2 MPa. As the cation size increase, P_d slightly decreases to 13.2 MPa for CsCl. This cation size effect should be associated with the small nanopore diameter. The average nanopore size of the MCM-41 under investigation is 2.1 nm. Without any confinement effect of solid surfaces, in bulk liquid phase a solvated cation is surrounded by a number of water molecules, forming a cluster through strong hydrogen bonds. The motion and the exchange of mass/energy with environment dominate the liquid transport behaviors. If the cation is Li⁺, its size is 0.076 nm. The molecular size of water is about 0.35 nm, and the van der Waals distance is around 0.3 nm. Thus, by accounting for the two water molecules on both sides of a cation, the characteristic length scale of the molecular cluster is smaller than the nanopore size. Under this condition, the configuration of the molecular cluster may not be disturbed much by the nanopore walls, as depicted by the dashed circles in Fig.K-3(a). If the cation is Cs⁺, since the ion size is quite large (~0.17 nm), the characteristic length scale of the molecular cluster is close to 1.5 nm, comparable with the nanopore size. If the van der Waals distance between the water molecules and the nanopore walls are taken into consideration, the nanopore size becomes insufficient for a fully developed solvated ion, as depicted in Fig.K-3(b). The testing data indicate that the repelling effect of the

nanopore surface to partly solvated large cations is lower than to fully solvated small cations, probably because that the system free energy is reduced when the cations are exposed to the solid surface.

At the equilibrium condition, the driving force and the resistance of infiltration are balanced with each other. The resistance is offered by the nanopore wall, which can be taken as $\gamma(2\pi r)$, where r is the nanopore radius and γ is the effective excess interfacial tension. The driving force of infiltration is caused by the pressure difference outside and inside the nanopores, which can be assessed as $P_{in} \cdot (\pi r^2)$. Thus, $\gamma = P_{in} \cdot r/2$. This mean-field analysis is consistent with the classic Laplace-Young equation. For the solutions of CsCl, KCl, NaCl, and LiCl, the values of γ are 17.3 mJ/m², 18.0 mJ/m², 18.9 mJ/m², and 19.6 mJ/m², respectively. The difference in system free energies of CsCl solution and LiCl solution is at the level of 2 mJ/m².

The confined liquid molecules does not diffuse out of the nanopores immediately when $P \cdot (\pi r^2)$ is smaller than $\gamma(2\pi r)$. The pressure must be over-decreased to nearly 20 MPa below P_{in} before defiltration begins, which may be caused by the additional resistance to molecular motion among tetrahedral sites of silyl groups. The liquid molecules and ions must overcome the energy barrier through thermal motion, and therefore when temperature increases defiltration becomes easier. During defiltration, since the most dominant factor is the relatively irregular nanopore surface features where a fully developed molecular cluster can be disrupted, the effect of cation size is suppressed. As a result, when the cation changes from Li⁺ to Cs⁺, the effective interfacial tension decreases from 7.6 mJ/m² to 6.6 mJ/m² by only 1 mJ/m², about one half of that in infiltration.

L. High-Speed Gas-Gun Experiment

The gas gun experiment was performed by using the UCSD 3-inch Cannon (Fig.L-1). A fully annealed brass ball (3/4" in diameter; 30.77 g in mass) was projected to the testing sample at the speed of 110 m/s. The output pulses were measured in the output bar. The experimental setup is depicted in Fig.L-2. A fully annealed brass ball was projected to the testing sample at the speed of about 110 m/s. The diameter of the brass ball was 3/4 inch; the mass was 30.77 g. The testing sample consisted of a stainless steel cylinder, in which the nanoporous materials functionalized (NMF) liquid was sealed by a hollow stainless steel piston. The piston was hollow so as to reduce the piston mass and the associated inertia effect. The piston and the cylinder was sealed by an reinforced Teflon o-ring. The NMF liquid contained about 6 g of liquid phase and 0.6 g of nanoporous particles suspended in it.

In the impact test, the piston acted as the input bar, and the NMF liquid was the medium through which the stress wave transmitted. The steel cylinder was tightly placed against a hardened aluminum alloy output bar, on which high-frequency strain gages were mounted, so that the output pulses were measured.

The first reference sample contained only pure water. The second reference sample contained only pure water, while the piston was protected by 10 g of polyurethane sheet. Sample "A" was based on nanoporous silica gel with the nanopore size of 7.8 nm. The material preparation procedure was the same as that described in Section H. Sample "B" was based on nanoporous MCM-41 with the nanopore size of 2.6 nm. The material preparation procedure was the same as that described in Section I. The testing results are shown in Fig.L-3. It can be seen clearly that the transmitted stress wave is largely reduced by the NMF liquid. Sample "A" absorbs 47% of the energy; sample "B" absorbs 63% of the energy.

M. Summary

In summary, through this three-year project, the mechanisms and processes that govern liquid behaviors in nanopores have been fundamentally much better understood. The major achievements include:

- (1) It has been validated in low-loading rate, gas-gun, and blast simulator experiments that nanoporous-materials-functionalized (NMF) liquids can be used in high-performance energy absorption systems. By applying an external pressure, liquid can be forced into the nanopores of a nonwetable material; as the ultralarge nanopore surface is exposed to the liquid phase, the system free energy increases significantly. The main advantages of NMF liquids include:
 - (a) the high energy absorption efficiency: the upper limit of this technique has been measured to be 140 J/g, compared to 50 mJ/g of Ti-Ni alloys and 1 J/g of composite materials;
 - (b) the high response frequency: the system performs well under high strain rates in gas gun and blast simulator tests; according to molecular dynamics simulations, the infiltration rate of liquid molecules in a nanopore is at the level of 1-10 m/s, and thus for a nanoporous particle with the size around 1-10 μm , the response frequency should be $10^6 - 10^8$ Hz; and
 - (c) the liquid nature of the materials, making it self-fitting to solid surfaces of complicated shapes or small-sized structures, fitting well with the recent progress of liquid-containing structures.
- (2) The NMF liquids have been used to enhance the performance of honeycomb structures. The energy absorption efficiency increases by a few times on volumetric basis as the cells are filled by the NMF liquid. On mass basis, the system performance increases by 20%.
- (3) A few nanoporous materials, including nanoporous silica gels, MCM41, nanoporous carbon, and zeolites have been identified to be suitable to the NMF liquid applications.
- (4) A set of surface treatment techniques have been developed to modified the inner nanopore surfaces of these materials, so that the working pressure can be adjusted in a broad range.
- (5) The effects of liquid composition, particular the liquid species (water, glycerin, solvents, liquid metal, etc.) and the electrolyte concentration, on infiltration pressure, infiltration volume, and defiltration behaviors have been systematically analyzed.
- (6) The feasibility of direct application of nanoporous structures as nanometer-scale honeycombs has been investigated experimentally. With the nm-scale defects (pores), the material exhibits significant plastic characteristics, leading to a large energy absorption efficiency. This mechanism can be combined with the liquid infiltration to further enhance the system performance.
- (7) Preliminary experiments were performed on energy-related applications of NMF liquids. When solvated ions are forced into the nanopores, at the large nanopore surface a large electrostatic charge can be generated, which is potentially useful for harvesting electricity from mechanical motions.
- (8) The fundamentals of behaviors of pressurized nanofluids have been much better understood. By using admixtures of size gradations, multiple-staged sorption isotherm curves can be obtained; the free volume between the nanopore wall and the solute molecules are directly measured. The influence of ion size and ion species on infiltration pressure and defiltration behavior is analyzed in considerable detail. Calometric measurement has been carried out to examine the heat generation associated with energy absorption of NMF liquids. In some systems, nearly all the mechanical work is converted to the solid-liquid interfacial tension, and the temperature variation is negligible. In other systems, the generated heat consists of an irreversible part and a reversible part. The former is related to the hysteresis of liquid motion, and the latter should be attributed to the energy barrier of tetrahedral sites.

Table A-1. Comparison of empty, water-filled, and NMF-liquid-enhanced cells.

	Mass, m (g)	Volume, V (cm ³)	Absorbed Energy (J)	U/m (J/g)	U/V (J/cm ³)
Empty Cell	0.57	0.94	6.54	11.5	6.96
Water-Filled Cell	1.48	0.94	5.80	3.92	6.17
NMF Liquid	1.20	0.94	16.7	13.9	17.8

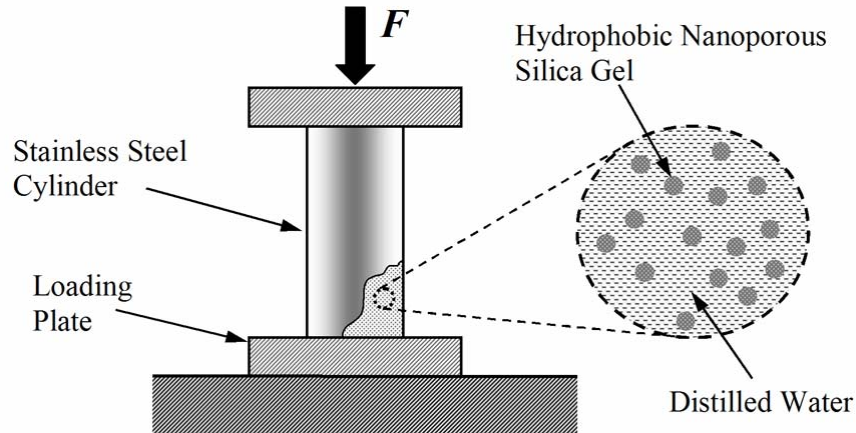


Fig.A-1 Experimental set-up.

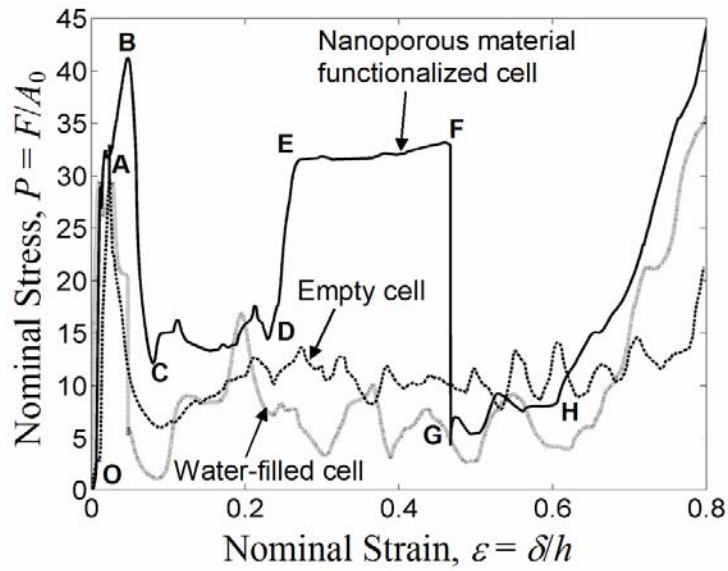


Fig.A-2 Measured buckling curves.

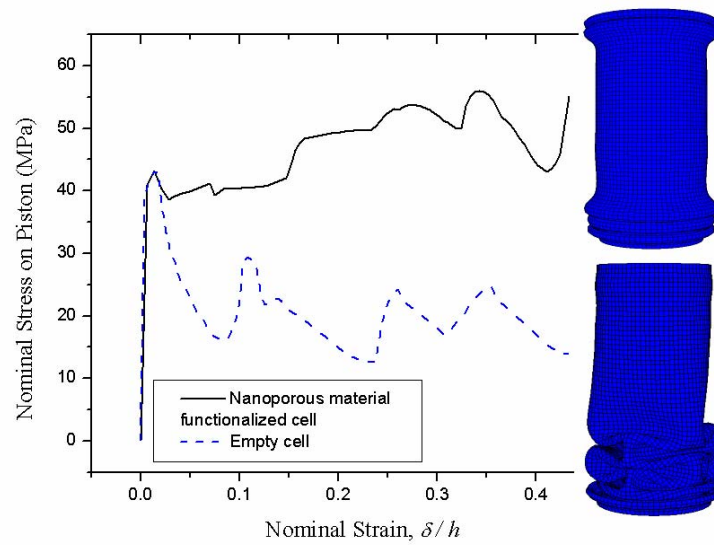


Fig.A-3 Simulated buckling curves.

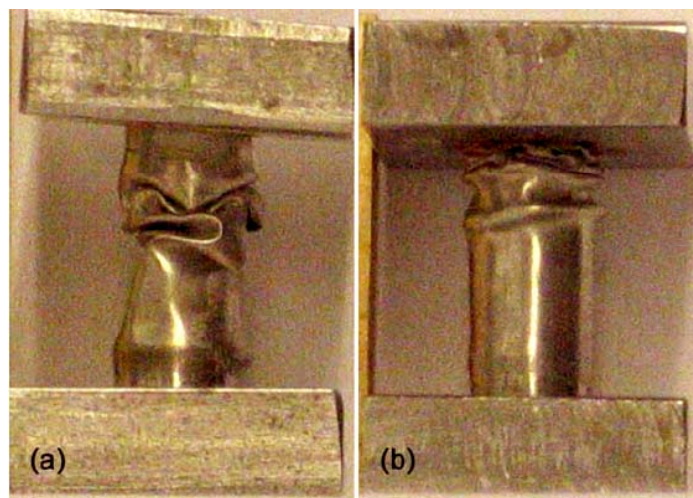
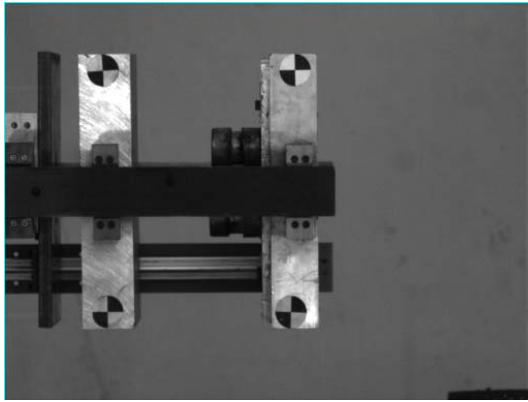
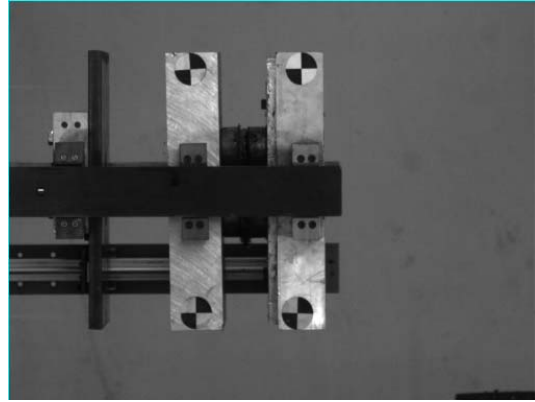


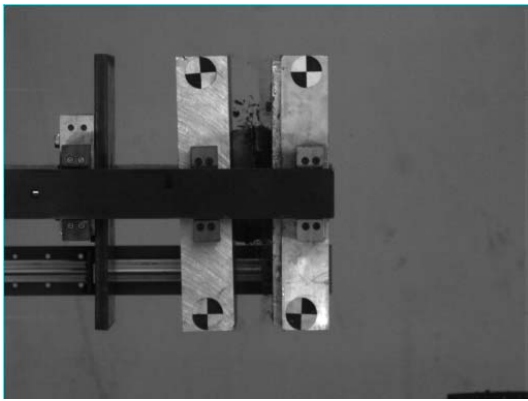
Fig.A-4 Photos of buckled steel cells: (a) an empty cell and (b) an cell filled by the NMF liquid.



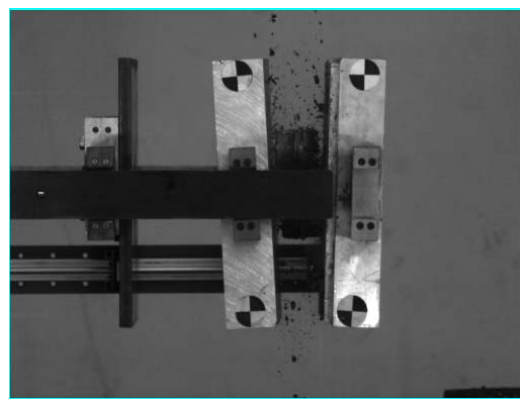
(a)



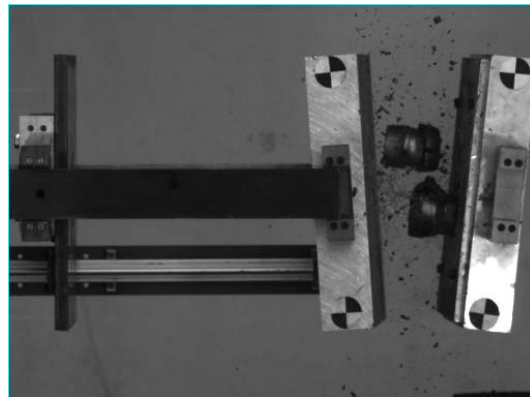
(b)



(c)



(d)



(e)

Fig.A-5 Blast simulator test on steel cells filled by a NMF liquid: (a) the projectile, which is a 30 kg aluminum alloy plate, is projected at a speed of 20 m/s; (b) the projectile hits the testing cells; (c) The cells are compressed (the debris are small pieces of epoxy glue); (d) the momentum is transmitted to the target plate; and (e) the projectile and the target plates move at about the same speed, indicating that the impact is nearly "perfectly plastic".

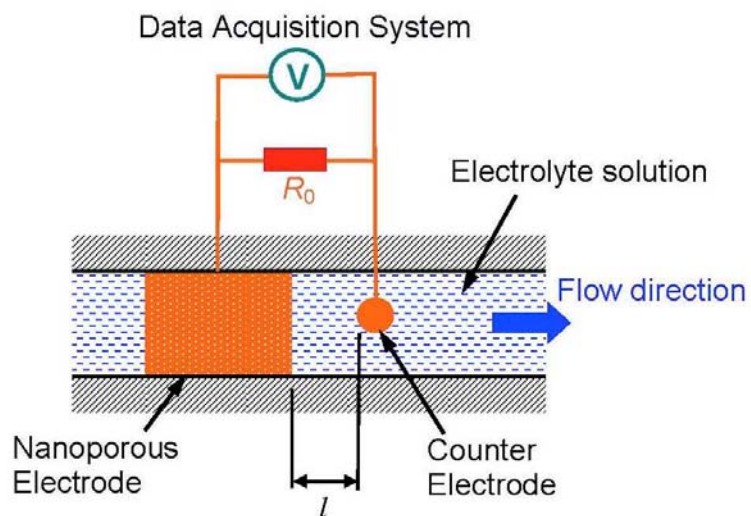


Fig.B-1 The experimental setup for mechanoelectric energy conversion.

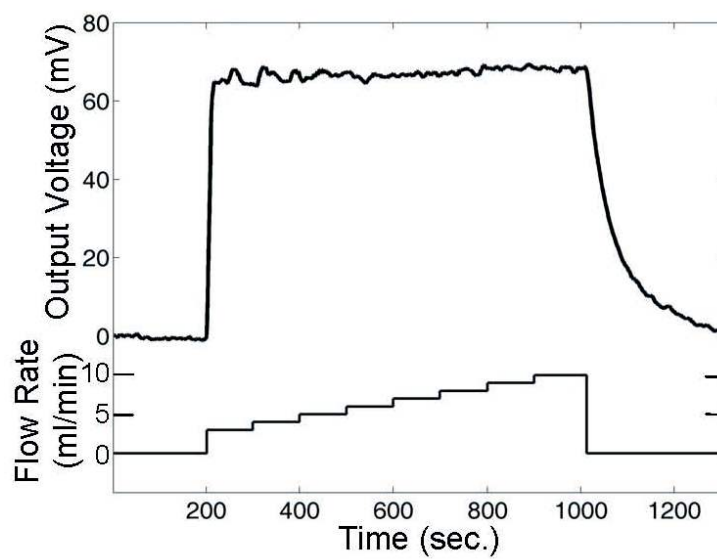


Fig.B-2 The output voltage as a function of the time.

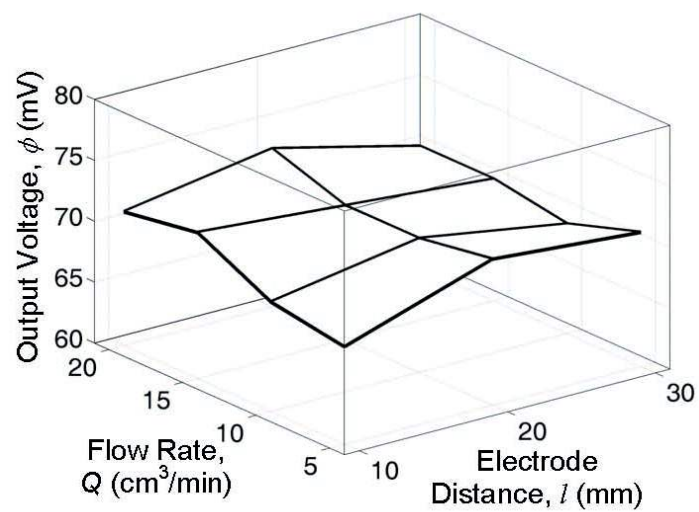


Fig.B-3 The output voltage as a function of the electrode distance and the flow rate.

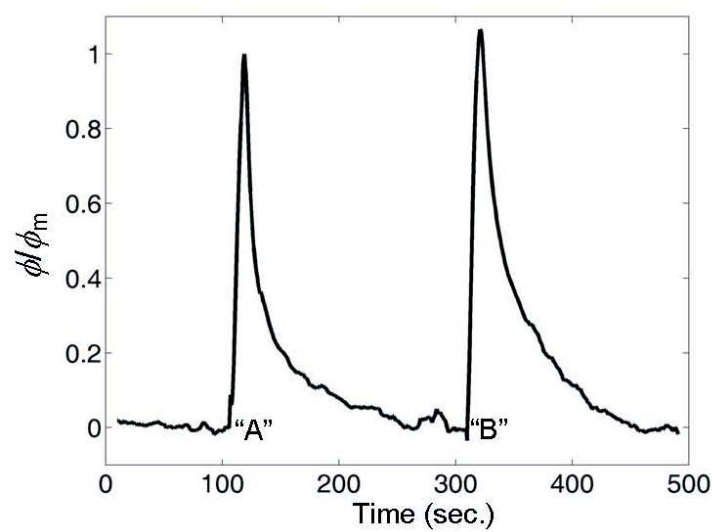


Fig.B-4 The decay of voltage and the system reactivation.

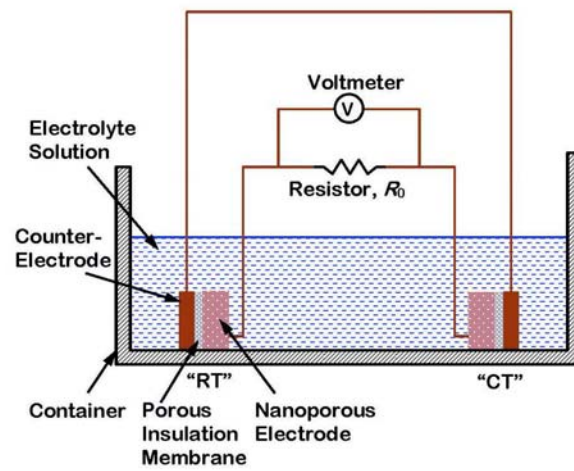


Fig.B-5 Thermoelectric experiment.

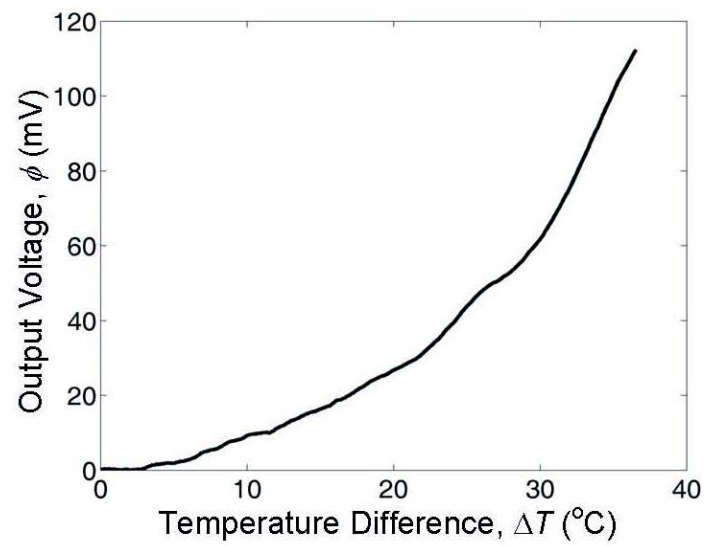


Fig.B-6 The output voltage as a function of the temperature difference.

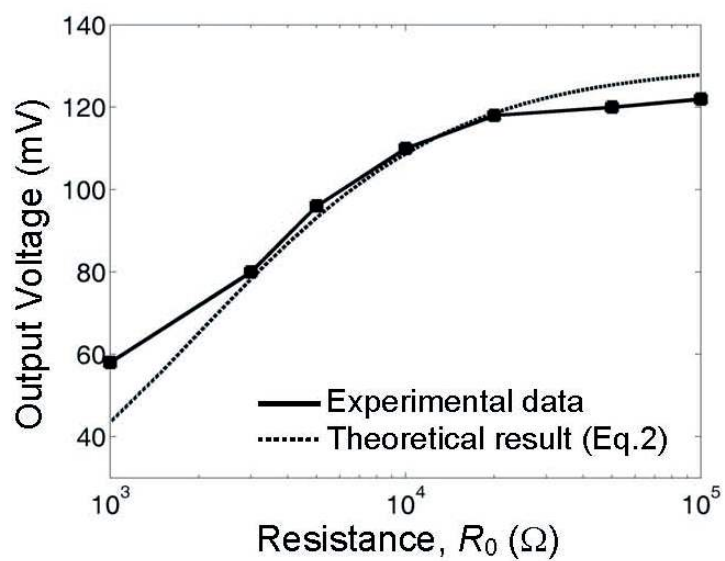


Fig.B-7 The output voltage as a function of the external resistance.

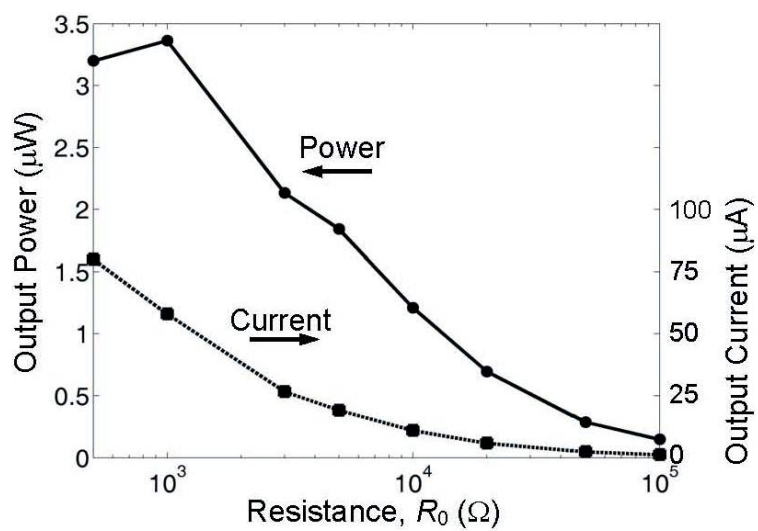


Fig.B-8 The output current and the output power.

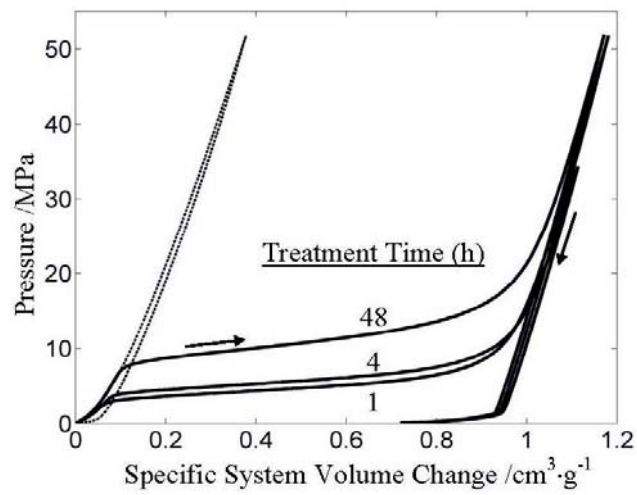


Figure C-1. Typical sorption isotherm curves of the first loading.
The dashed line indicates the reference curve.

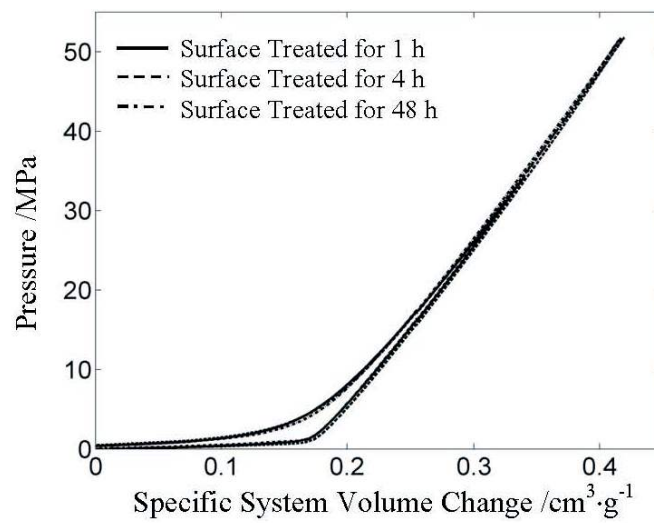


Figure C-2. Sorption isotherm curves of the second loading.

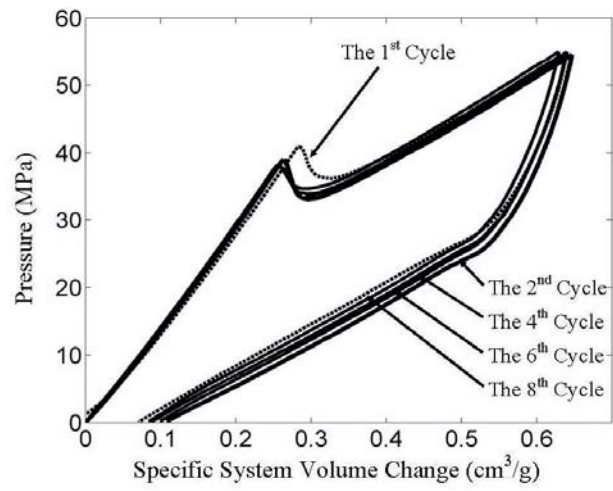


Fig.D-1 Low-pressure sorption isotherm curves.

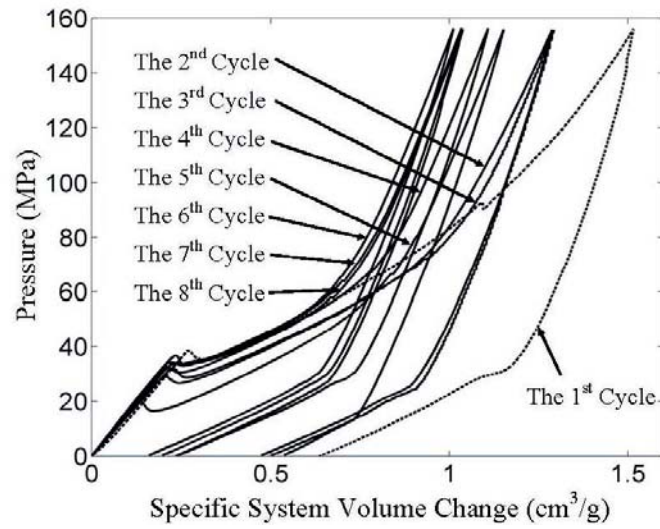


Fig.D-2 High-pressure sorption isotherm curves.

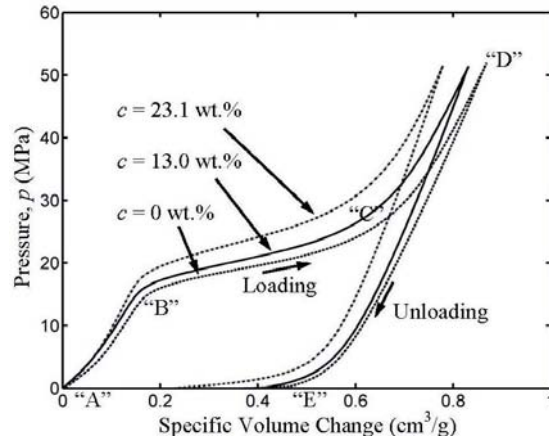


Fig. E-1 Sorption isotherm curves of NaCl modified system.

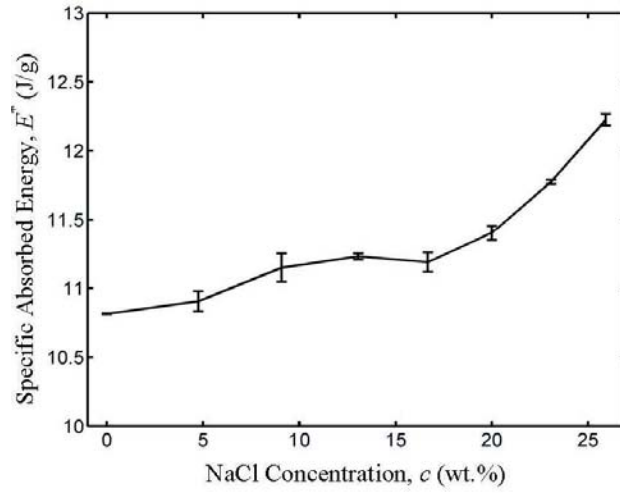


Fig.E-2 Energy absorption capacity as a function of [NaCl].

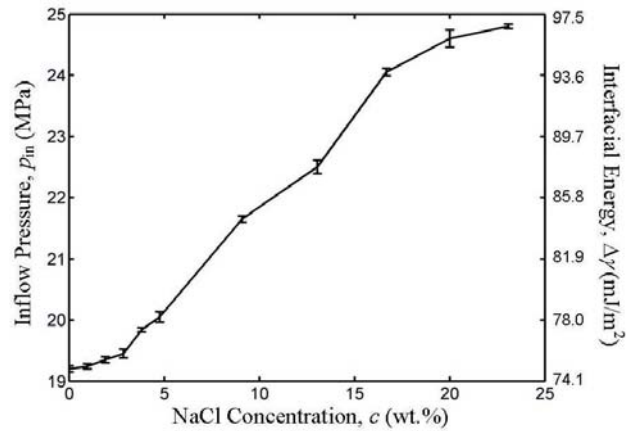


Fig.E-3 Infiltration pressure as a function of [NaCl].

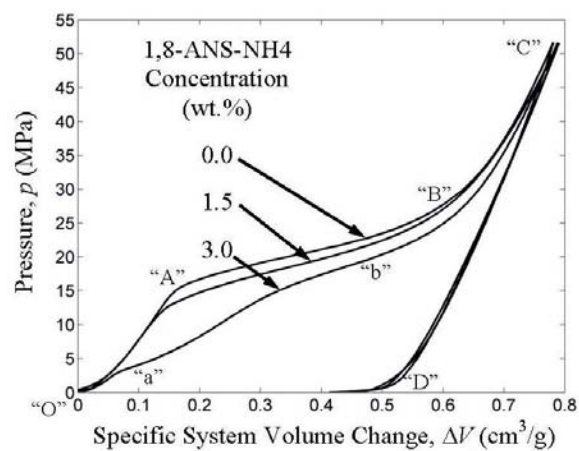


Fig.E-4 Sorption isotherm curves of systems without CSH.

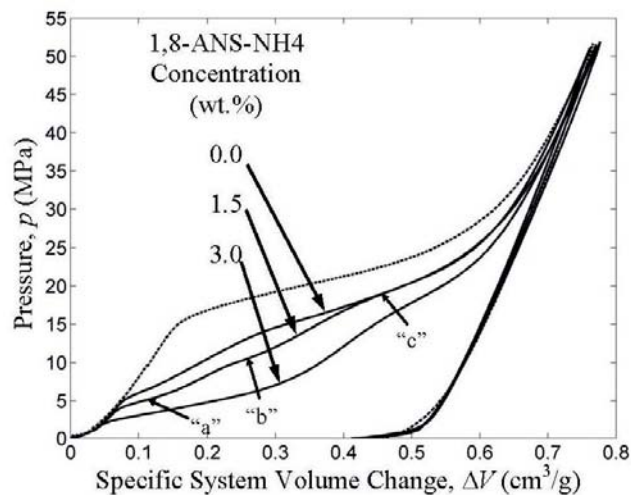


Fig.E-5 Sorption isotherm curves of systems with [CSH] = 1.5%.

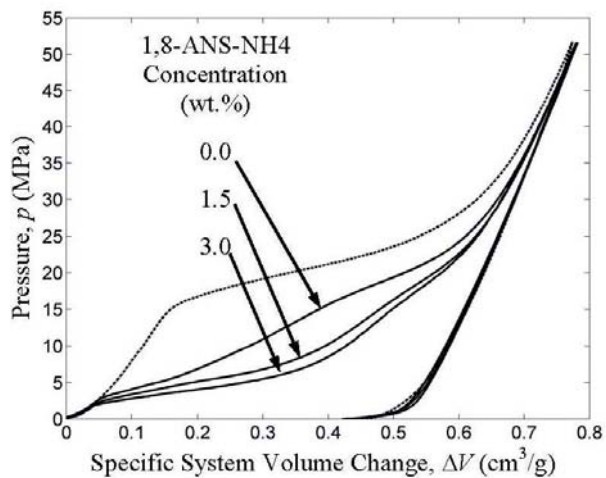


Fig.E-6 Sorption isotherm curves of systems with [CSH] = 3%.

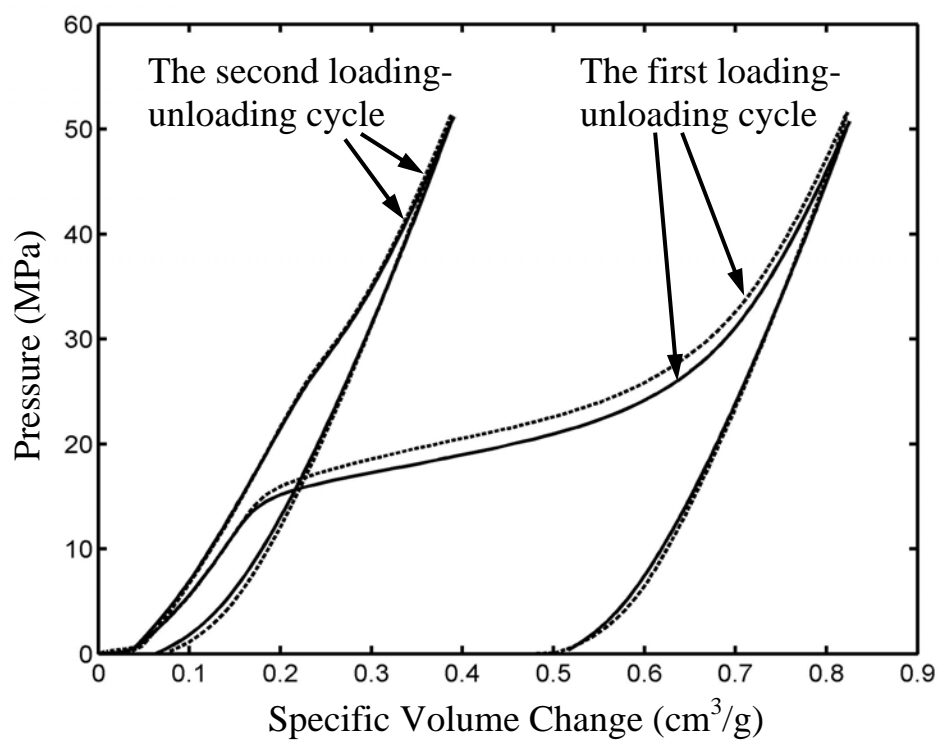


Fig.F-1 Sorption isotherm curves of the system modified by PIMA-Na.

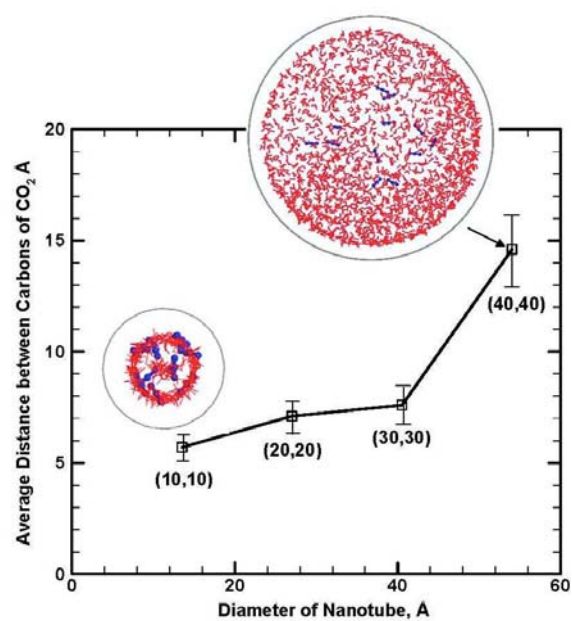


Fig.G-1 Average distance among confined liquid molecules.

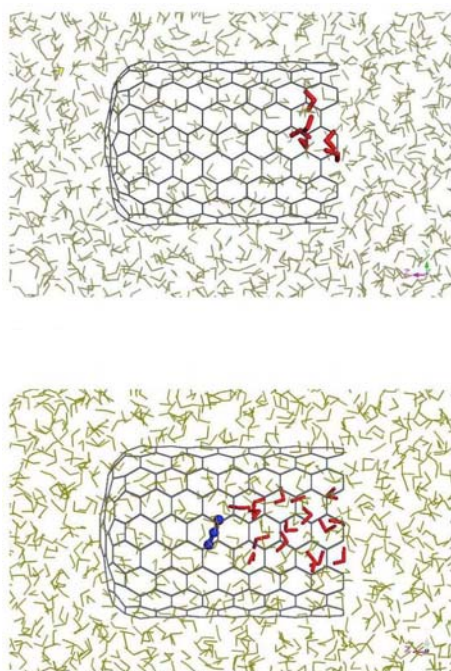


Fig.G-2 Infiltration of liquid molecules (a) without and (b) CO₂ molecule.

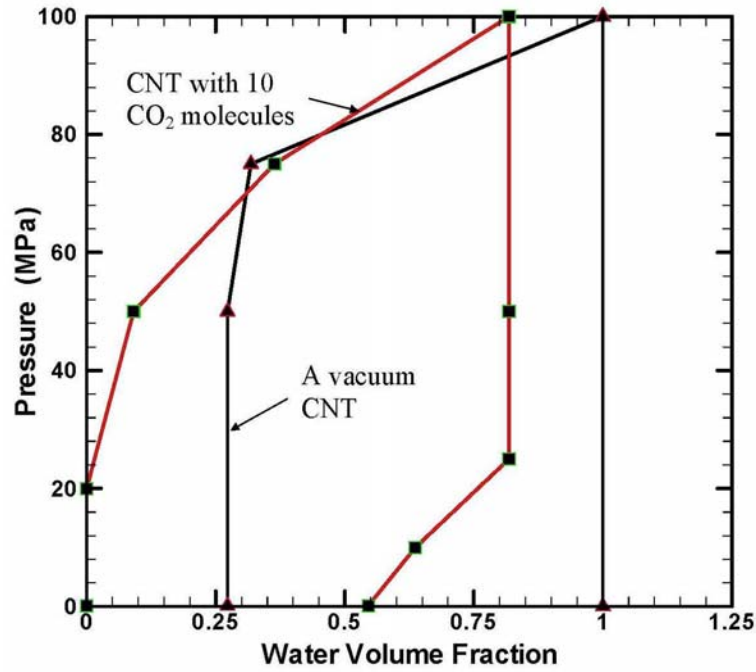


Fig.G-3 Calculated sorption isotherm curve.

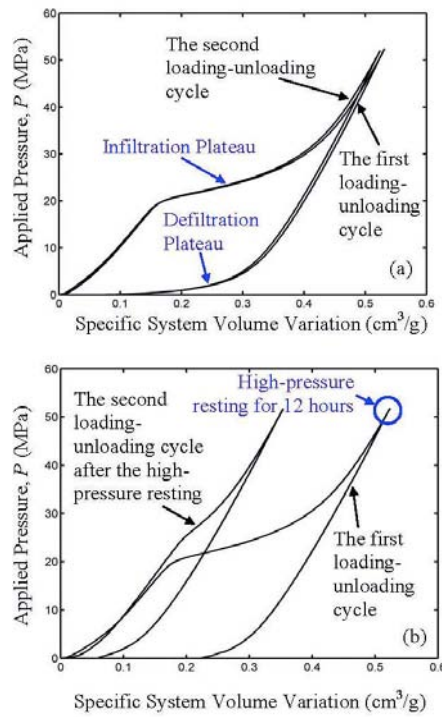


Fig.G-4 Measured sorption isotherm curves: (a) without and (b) with high-pressure resting.

Table H-1 Results of the Calometric Measurement ($^{\circ}\text{C}$).

Test	Stage of Infiltration			
	Onset of loading ("A")	Onset of infiltration ("B")	Onset of Unloading ("C")	End of unloading ("D")
1	23.5	23.6	23.6	23.4
2	23.4	23.4	23.5	23.5
3	23.3	23.5	23.7	23.7
4	23.5	23.5	23.5	23.6
Average	23.4	23.5	23.5	23.5
5 *	23.5	—	23.7	23.6
6 *	23.4	—	23.5	23.6
Average	23.4	—	23.6	23.6

* Tests 5 and 6 are for the reference system that contains only 5 g of deionized water.

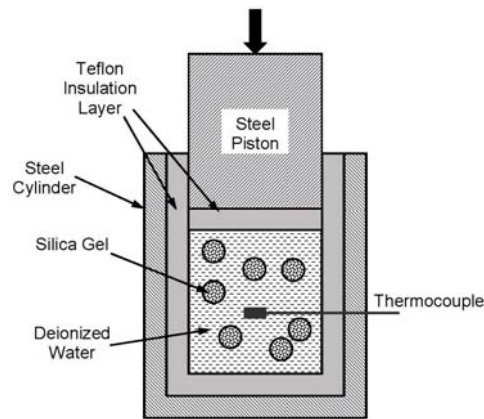


Fig.H-1 Schematic of the calometric measurement system.

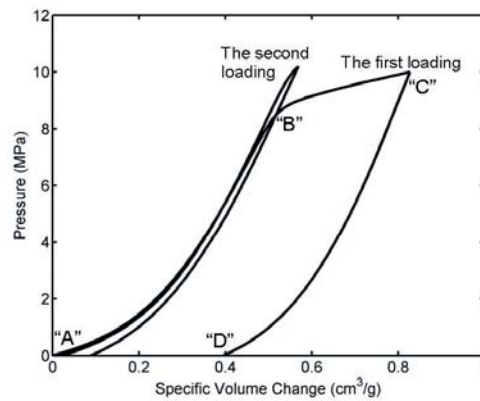


Fig.H-2 Typical sorption curves.

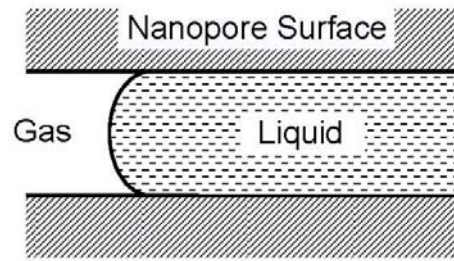


Fig.H-3 Schematic of the confined liquid in a nanopore.

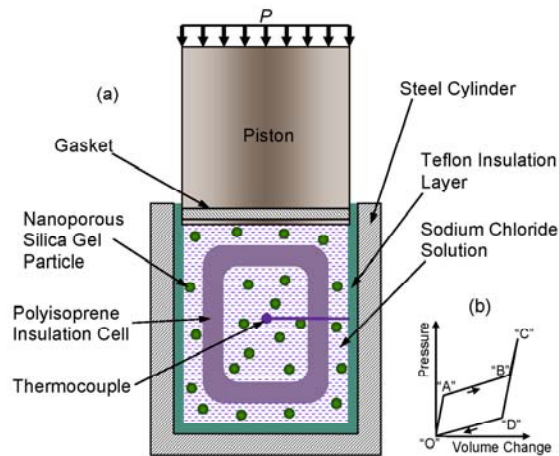


Fig.H-4 Schematic diagrams of (a) the experimental setup and (b) the sorption curve.

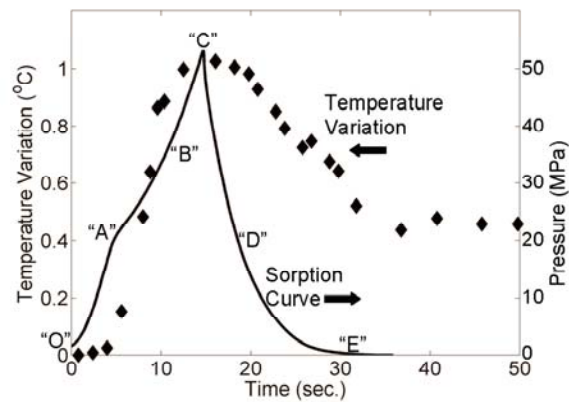


Fig.H-5 The temperature and the pressure profiles of a system containing 750 mg of silica gel. The loading rate is 8 mm/min.

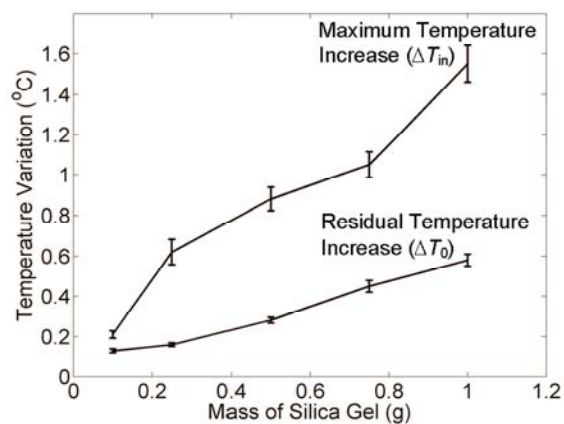


Fig.H-6 The temperature variation as a function of the mass of silica gel. The loading rate is 2 mm/min.

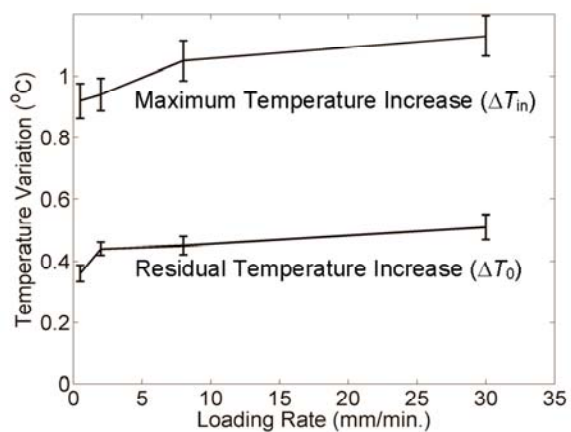


Fig.H-7 The temperature variation as a function of the loading rate. The mass of silica gel is 750 mg.

Table I-1. The infiltration behaviors of MCM41 with mercury.

	Mass Density (g/cm ³)	Infiltration Pressure (MPa)	Effective Porosity (cm ³ /g)	Energy Dissipation Effectiveness (J/g)
The first loading cycle	0.4	102	0.8	140
The second loading cycle	11	104	0.05	4

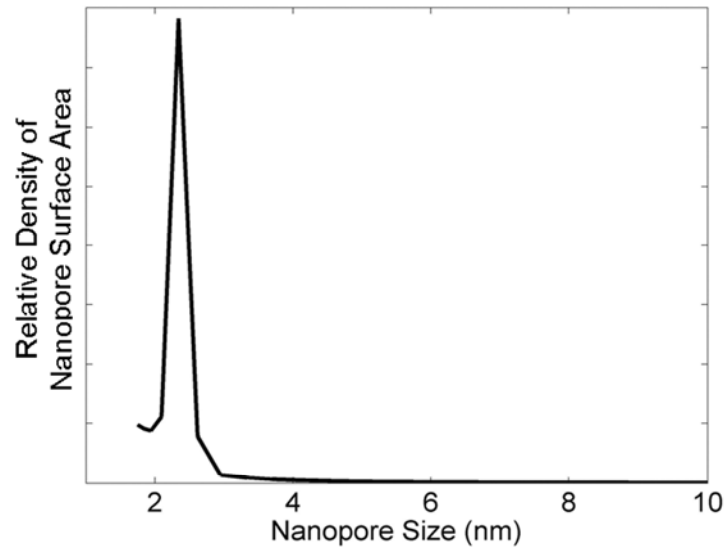


Fig. I-1 The distribution of nanopore size.

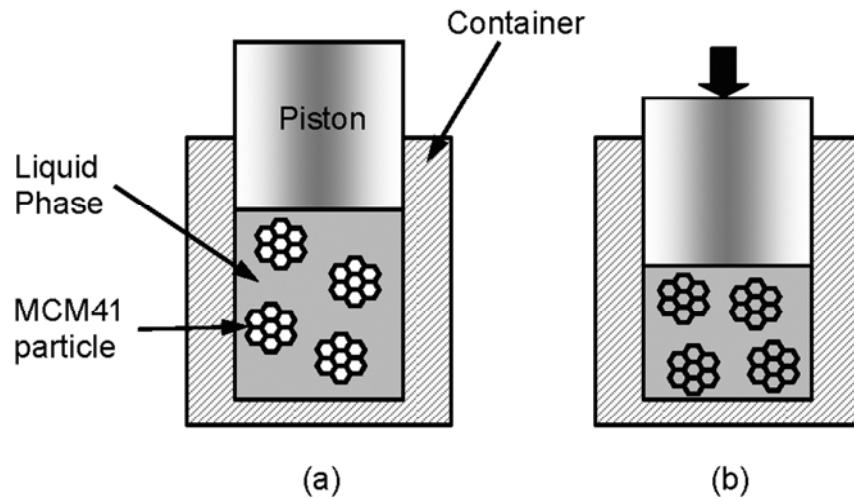


Fig. I-2 The experimental setup: (a) prior to and (b) after the pressure induced infiltration test.

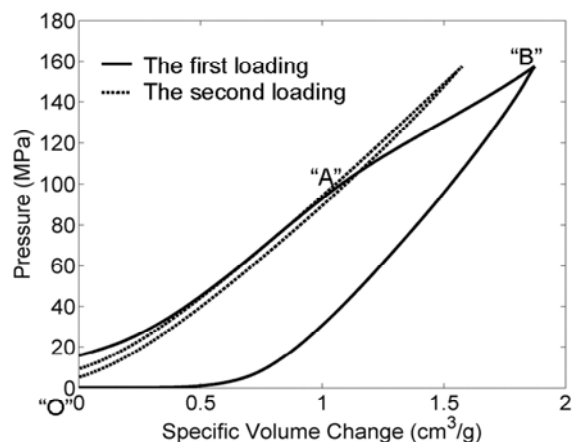


Fig. I-3 Typical sorption isotherm curves. The maximum pressure is set to 160 MPa. The curves have been shifted along the horizontal axis so that the tangents of lower-pressure linear sections pass through the origin ("O").

Table J-1 The nanoporous structures of the silica samples before and after the compression tests.

	Average nanopore radius (nm)	Specific nanopore surface area (m ² /g)	Specific nanopore volume (cm ³ /g)	Weight density (mg/cm ³)
Before compression test	5.4	272	0.54	742
After being compressed at 200 MPa	5.3	272	0.53	761
After being compressed at 750 MPa	4.7	267	0.34	1128

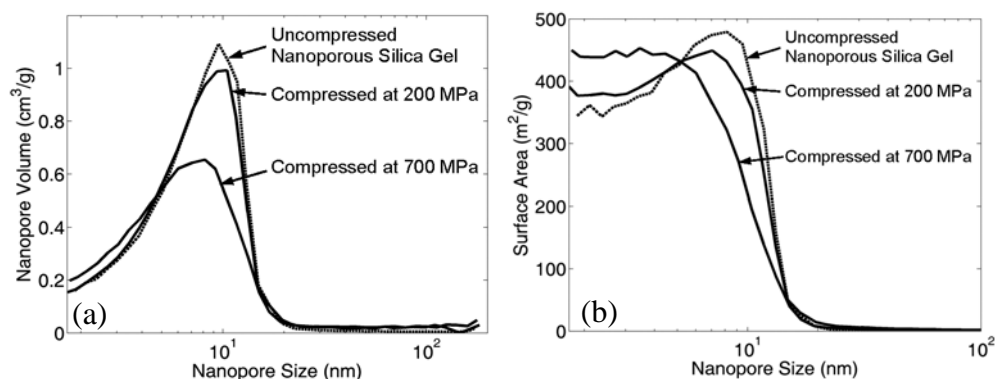


Fig.J-1 Gas absorption analysis results of the nanoporous silica gel sample: (a) the nanopore volume distributions and (b) the nanopore surface area distribution.

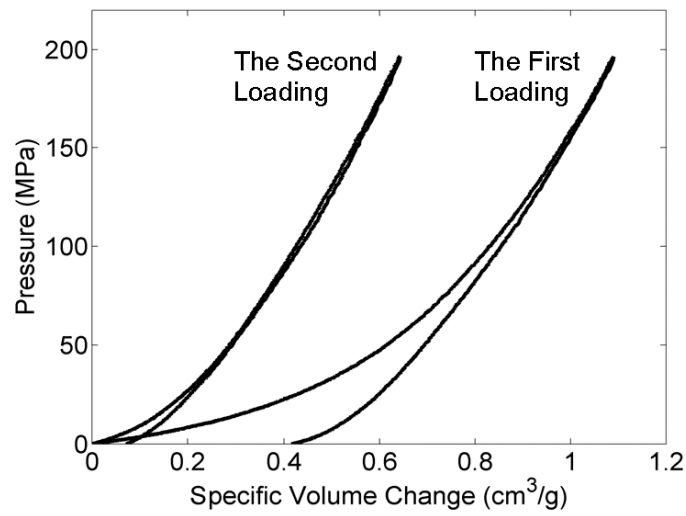


Fig.J-2 Typical load-displacement curves of a low-pressure test. The curves have been shifted horizontally.

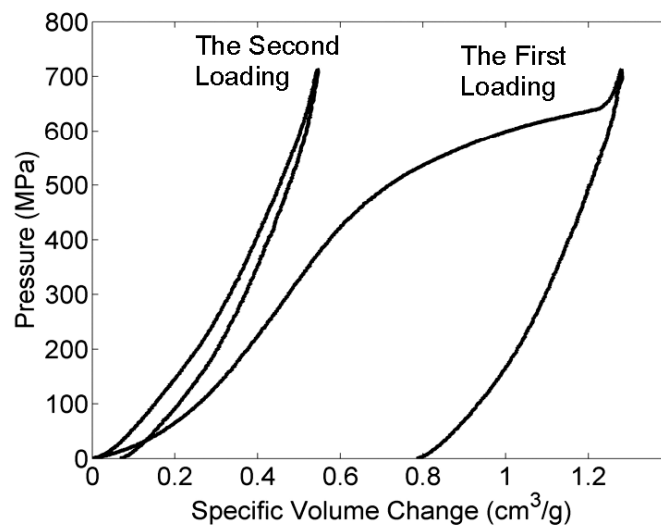


Fig.J-3 Typical load-displacement curves of a high-pressure test. The curves have been shifted horizontally.

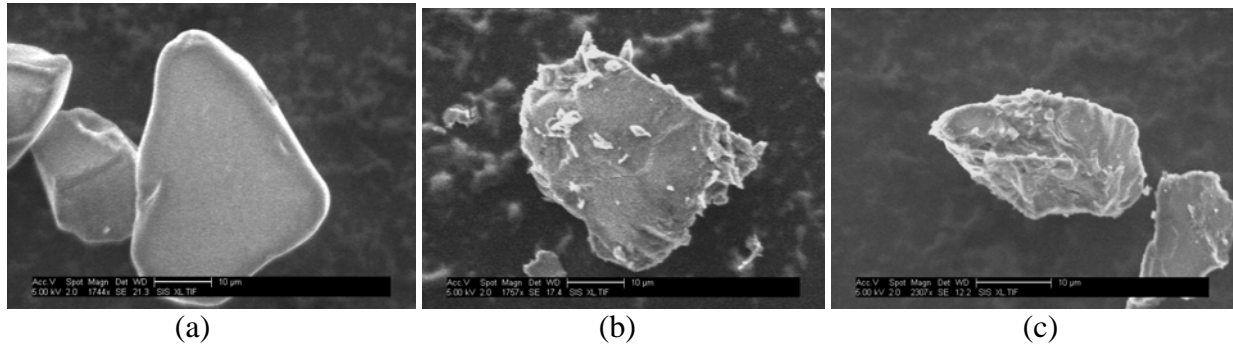


Fig.J-4 Typical SEM microscopy of silica particles (a) before the compression test; (b) after the low-pressure compression test; and (c) after the high-pressure compression test.

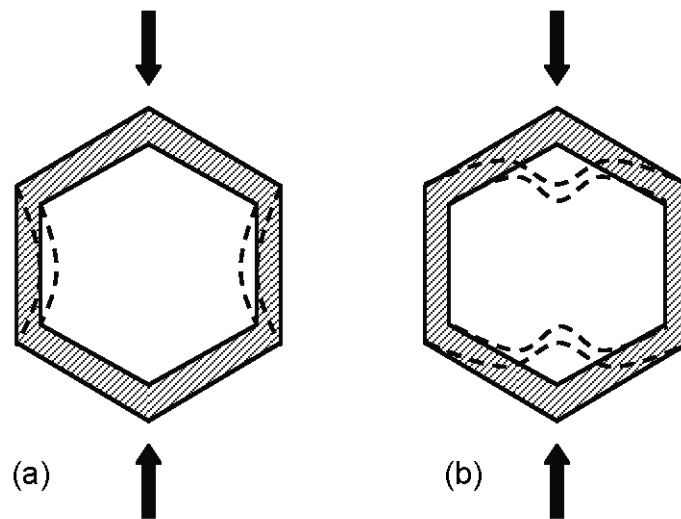


Fig.J-5 Schematic of possible failure modes of nanopore walls: (a) parallel and (b) normal to the external loading. The arrows indicate the direction of external loading.

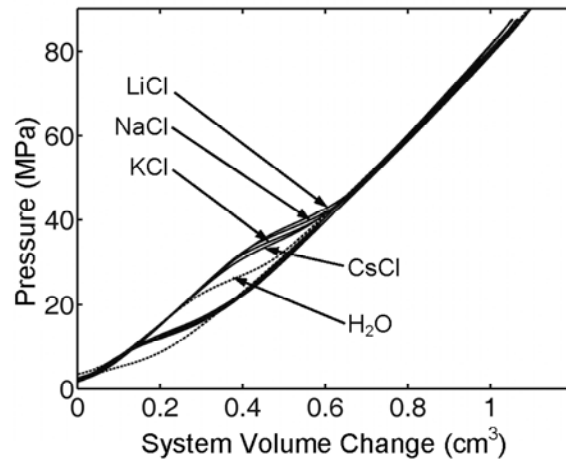


Fig.K-1 Typical sorption curves of various electrolyte solutions. The dashed line indicates the behavior of the pure water based system.

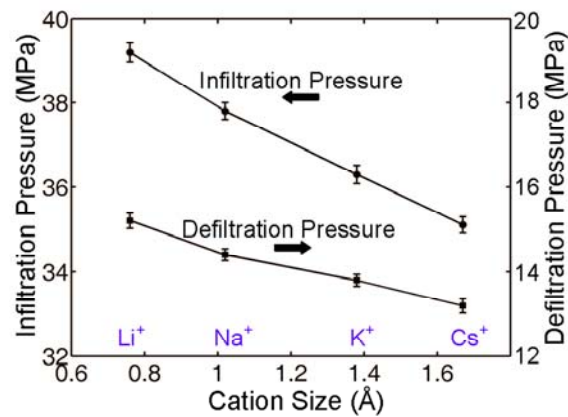


Fig.K-2 The influence of the cation size on the infiltration and defiltration pressures.

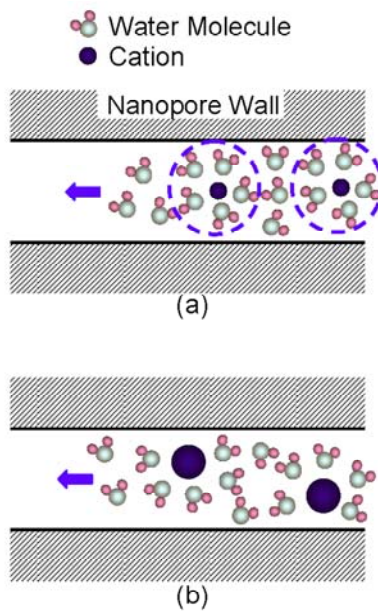


Fig.K-3 Schematic of the infiltration process of (a) relatively small and (b) relatively large ions in a nanopore. The anions are not shown.



Fig.L-1 A photo of the gas gun.

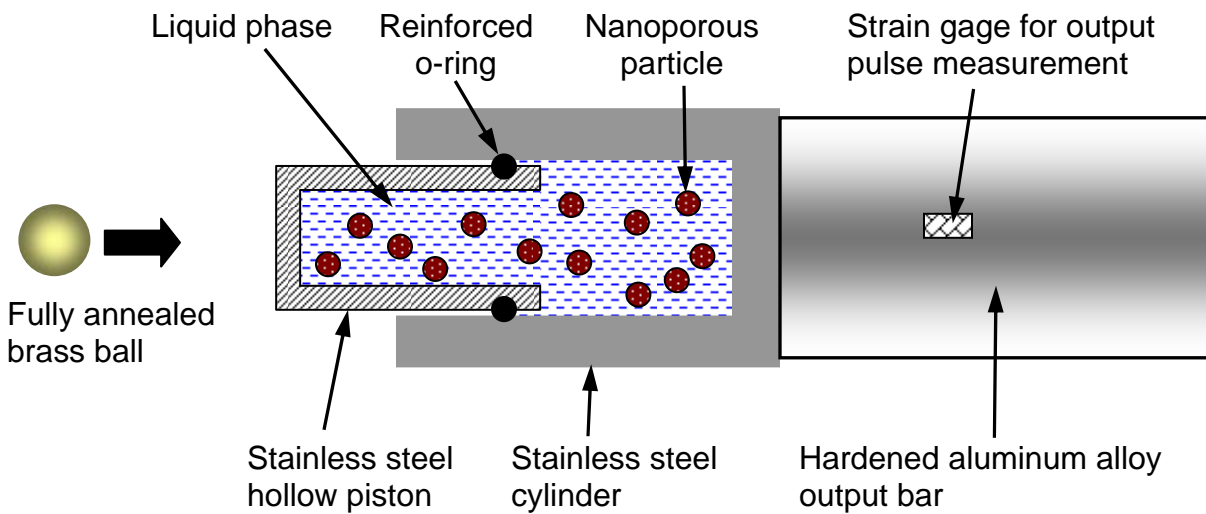


Fig.L-2 Schematic of experimental setup.

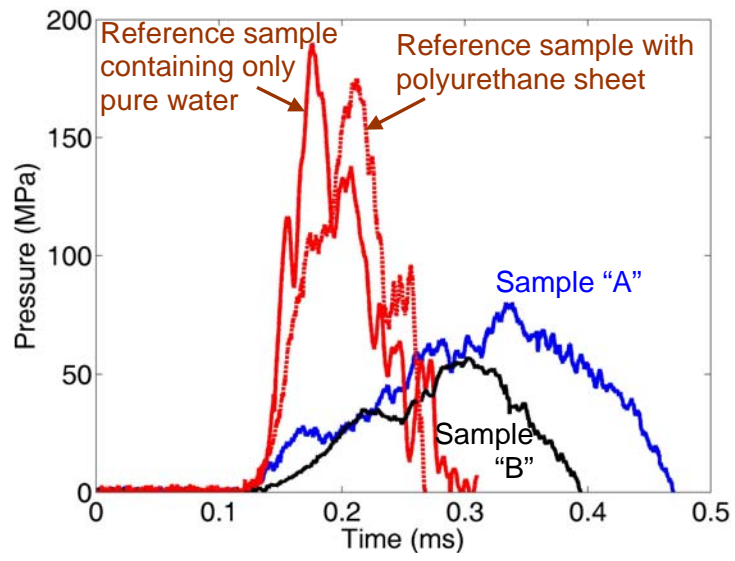


Fig.L-3 Measurement results